TITLE

Afadin-deficient retinas exhibit severe neuronal lamination defects but preserve visual functions

Akiko Ueno[abd#], Konan Sakuta[c#], Hiroki Ono[b], Aki Hashio[c], Haruki Tokumoto[c], Mikiya Watanabe[c], Taketo Nishimoto[c], Toru Konishi[b], Yuki Emori[c], Shunsuke Mizuno[c], Mao Hiratsuka[c], Jun Miyoshi[e], Yoshimi Takai[f], Masao Tachibana[a], Chieko Koike[abd]

[a]Center for Systems Vision Science, Research Organization of Science and Technology, Ritsumeikan University, Kusatsu, Shiga 525-8577, Japan,
[b]College of Pharmaceutical Sciences, Ritsumeikan University, Kusatsu, Shiga 525-8577, Japan,
[c]Graduate School of Pharmacy, Ritsumeikan University, Kusatsu, Shiga 525-8577, Japan,
[d]Ritsumeikan Global Innovation Research Organization (R-GIRO), Ritsumeikan University, Kusatsu, Shiga 525-8577, Japan,
[e]Department of Molecular Biology, Osaka Medical Center for Cancer and Cardiovascular Disease, Osaka, Japan.
[f]Division of Pathogenetic Signaling, Department of Physiology and Cell Biology, Kobe University Graduate School of Medicine, Kobe, Hyogo, Japan.
# These authors contributed equally to this work.

Corresponding author

Chieko Koike, Ph.D.

koike@fc.ritsumei.ac.jp

ABSTRACT

Neural lamination is a common feature of the central nervous system (CNS), with several subcellular structures, such as adherens junctions (AJs), playing a role in this process. The retina is also heavily laminated, but it remains unclear how laminar formation impacts retinal cell morphology, synapse integrity, and overall retinal function. In this study, we demonstrate that the loss of afadin, a key component of AJs, leads to significant pathological changes. These include the disruption of outer retinal lamination and a notable decrease as well as mislocalization of photoreceptors, their outer segments, and photoreceptor synapses. Interestingly, despite these severe impairments, we recorded small local field potentials, including the a- and b-waves. We also classified retinal ganglion cells (RGCs) into ON, ON-OFF, and OFF types based on their firing patterns in response to light stimuli. Additionally, we successfully characterized the receptive fields of certain RGCs. Overall, these findings provide evidence that retinal circuit function can be partially preserved even when there are significant disruptions in both retinal lamination and photoreceptor synapses. Our results indicate that retinas with severely altered morphology still retain some capacity to process light stimuli.

INTRODUCTION

A common feature of the central nervous system (CNS) in vertebrates is highly laminated structures, which are established by well-ordered neuronal migration (Ayala et al., 2007; Liu, 2011; Veeraval et al., 2020). Lamination defects are observed in some patients with psychiatric disorders, such as autism spectrum disorder, and these rodent models suggest that lamination may be associated with neural circuit formation and function (Miao et al., 1994; Pan et al., 2019; Romero et al., 2018; Stouffer et al., 2016). However, several studies report that orderly lamination is dispensable for the assembly of direction-selective tectal circuits as well as for several cortical circuit functions and synaptic connections (Dräger, 1981; Guy et al., 2015; Guy and Staiger, 2017; Nikolaou and Meyer, 2015). Therefore, the full extent of the association between lamination and the integrity of neural circuit function remains elusive.

Adherens junctions (AJs), known to be correlated with CNS lamination, are adhesive intercellular junctions composed of protein complexes that mediate strong cell-cell adhesion (Harris and Tepass, 2010; Masai et al., 2003; Meng and Takeichi, 2009; Park et al., 2002; Takai et al., 2008b). Cadherin-catenin complex, nectin-afadin complex, and actin cytoskeleton are the major components of AJs (Gil-Sanz et al., 2014; Harris and Tepass, 2010; Ikeda et al., 1999; Meng and Takeichi, 2009; Tachibana et al., 2000; Takai et al., 2008b, 2008a). Cell-cell adhesion of AJs is mainly mediated by the cadherin-catenin complex, whereas nectin and afadin are required for the initial establishment of AJs (Takai and Nakanishi, 2003). A recent report shows that afadin in intestinal

cells is essential for epithelial cell-cell adhesion which was previously assumed to be primarily regulated by cadherin and catenin (Mangeol et al., 2024). Following this result, the functional importance of afadin and nectin in AJs is being reconsidered (Sebbagh and Schwartz, 2024). Animals with mutations in AJ molecules exhibit cell migration defects in the developing stage, resulting in disruption of lamination, which might be associated with brain dysfunctions, such as intellectual disability (Baum and Georgiou, 2011; de Ligt et al., 2012). However, how the defects in AJs affect the CNS function also remains unclear.

The retina, one of the best-understood mammalian neural circuits in the CNS, is highly laminated and organized into three nuclear layers and two synaptic layers (Amini et al., 2017). In the retina, incoming light is converted into neural signals in photoreceptors, processed in parallel through a network of interneurons, and finally sent to the brain via the optic nerve, the bundle of retinal ganglion cell (RGC) axons (Masland, 2012). Photoreceptors, bipolar cells (BCs), and RGCs are connected sequentially, and horizontal cells and amacrine cells (ACs) modulate the information flow in the circuit (Wässle, 2004). The mechanisms underlying retinal circuit formation and function have been actively studied, but the effects of retinal lamination disruption on retinal neural circuits remain unclear (Duan et al., 2018, 2014; Gollisch and Meister, 2010; Zapp et al., 2022). In mammals, most of the major AJ molecules belong to protein families, possibly resulting in functional redundancy with no apparent lamination phenotype in a single knockout (KO) of a member of this complex. Indeed, the loss of central AJ molecules, nectin-1 and nectin-3, does not cause severe

106 defects in retinal lamination (Inagaki et al., 2005). To clarify the effects of AJ
107 molecule depletion on retinal neural circuits and cell morphology while avoiding
108 the issue of functional redundancy, we focused on afadin, which is a scaffolding
109 protein for nectin and has no paralog in mice. Afadin regulates the localization
110 of nectin, which initiates cell–cell adhesion and promotes AJ formation by
111 recruiting the cadherin–catenin complex. (Ohama et al., 2018; Takai and
112 Nakanishi, 2003). In addition, afadin interacts with various cell adhesion and
113 signaling molecules, as well as the actin cytoskeleton, and contributes to the
114 accumulation of β-catenin, αE-catenin, and E-cadherin at AJs (Sakakibara et
115 al., 2018; Sato et al., 2006). *Afadin* KO mice exhibit severe disruption of AJs in
116 the ectoderm, along with other developmental defects, leading to embryonic
117 lethality (Ikeda et al., 1999; Zhadanov et al., 1999). Conditional deletion of
118 afadin in RGCs leads to disruption of dendrites in ON-OFF direction-selective
119 RGCs (Duan et al., 2018). However, the effect of afadin loss on retinal
120 lamination, circuit formation, and function is poorly understood.
121
122 In this study, using the *afadin* conditional KO (cKO) mouse, we revealed that the
123 *afadin*-deficient retinas exhibit severe pathological defects, such as outer retinal
124 lamination disruption, as well as decrease and mislocalization of photoreceptors
125 and their synapses. In contrast to severe disruption of the outer retina, the inner
126 plexiform layer (IPL) structure in the inner retina was relatively intact. Using the
127 retinas isolated from the *afadin* cKO mouse, we could record local field
128 potentials (micro electoretinograms: mERGs) and RGC firings. Based on the
129 light-evoked firing pattern, RGCs could be classified into ON, ON-OFF, OFF,

and other types as previously established. Furthermore, the receptive field (RF) could be mapped in some RGCs. Consistent with this, the cKO mice responded to moving stimuli in visual behavioral tests. Our results suggest that neural circuits in the retina with severe defects of the outer retinal lamination and photoreceptor synapses can mediate some visual information processing and partially preserve visual functions.

MATERIALS and METHODS

Animals

All animal experimental protocols were conducted in accordance with local guidelines and the ARVO statement on the use of animals in ophthalmic and vision research. These procedures were approved by the Institutional Safety Committee on Recombinant DNA Experiments (approval ID R4016) and Animal Experimental Committees (approval ID BKC2022-017) of Ritsumeikan University. Mice were kept in the temperature-controlled room at 25°C with a 12 h/12 h day/night cycle. Fresh water and rodent diets were always provided.

WT, *afadin* conditional heterozygous (cHet), and cKO mice on 129S6/SvEvTac background, and *R26R-H2B-EGFP* mice on C57BL/6J background were used in this study. The *afadin flox* mice (Majima et al., 2009), *Dkk3-Cre* mice (Sato et al., 2007; Yamamoto et al., 2020), and *R26R-H2B-EGFP* mice (Abe et al., 2011,CDB Accession number. CDB0203K), have been described previously. Exon 2 of the *afadin* gene is flanked by loxP sites in the *afadin flox* mice, and Cre activity is detected in the retina of the *Dkk3-Cre* mice from embryonic day 10.5 (E10.5). Mice of either sex were used for all animal experiments. The stages used for individual experiments are described in figure legends.

Immunohistochemistry

Immunohistochemical analysis was performed as described previously (Hori et al., 2019; Kubo et al., 2021). In brief, the retina used for MEA recordings and isolated mice eyes were fixed with 4% PFA in PBS for 30 min at room

162 temperature. After three-time washes, retinas were cryoprotected by 30%
163 sucrose in PBS overnight, embedded in an OCT compound (Sakura, Japan),
164 frozen on dry ice, and sectioned at 20 μm of thickness. Whole-mount
165 immunostaining was performed as previously described with some
166 modifications (Ueno et al., 2018). The retinas were gently peeled off from the
167 sclera, fixed with 4%PFA in PBS for 30 min at room temperature, and washed
168 three times. Retinal sections and whole retinas were soaked in blocking buffer
169 (5% NDS, 0.1% Triton X-100, in 1x PBS) for 1-2 h at room temperature, and
170 incubated with primary antibodies in blocking buffer 1 or 2 overnight at 4°C. The
171 sections were washed with PBS three times and incubated with fluorescent dye-
172 conjugated secondary antibodies and DAPI (1:1000) for more than 2 h at room
173 temperature or overnight at 4°C under the light-shielded condition. The
174 specimens were observed using a laser confocal microscope (LSM900; Carl
175 Zeiss, Germany). For BrdU staining, mice were given an intraperitoneal
176 injection of 20 mg/kg BrdU and sacrificed 2 h later. Retinal sections were then
177 pretreated with 2 N HCl at 37 °C for 30 min before blocking. The antibodies and
178 dilution ratios were as follows; anti-l-afadin (ab90809, Abcam, UK, 1:100), anti-
179 nectin1 (D146-3, MBL, Japan, 1:100), anti-nectin2 (D083-3, MBL, Japan,
180 1:100), anti-nectin3 (D084-3, MBL, Japan, 1:100), anti-PKCα (P5704, Sigma,
181 USA, 1:1000, P4334, Sigma, 1:10000), anti-SCGN (AF4878, R&D systems,
182 USA, 1:2000), anti-Arr3 (AB15282, Millipore, USA, 1:1000), anti-Calbindin
183 (PC253L-100, Millipore, USA,1:200), anti-ChAT (AB144P, Millipore, USA, 1:50),
184 anti-Bassoon (SAP7F407, Enzo, USA, 1:1000), anti-mGluR6 (current study,
185 1:3000), anti-PSD95 (#124 014, Synaptic Systems, Germany, 1:3000), anti-

186 GluR5 (Grik1, gift from Steve H DeVries, 1:2000), anti-PKARIIβ (#610625, BD
187 biosciences, USA, 1:500), anti-Calretinin (PC235L-100UCN, Millipore, USA,
188 1:5000), anti-EAAT5 (HPA049124, Sigma, USA, 1:100), anti-vGlut1 (AB5905,
189 Millipore, USA, 1:6000), anti-HPC-1 (S0664, Sigma, USA, 1:10000), anti-active
190 caspase3 (AF835, R&D Systems, USA, 1:300), anti-Chx10 (Hori et al., 2019,
191 1:100), anti-Otx2 (AF1979, R&D systems, USA, 1:200), anti-Glutamine
192 synthetase (GS, MAB302, Millipore, USA, 1:500), anti-CD31 (#557355, BD
193 Biosciences, USA, 1:100), anti-Lhx2 (sc-19344, Santa Cruz Biotechnology,
194 USA, 1:100), anti-RBPMS (GTX118619, GeneTex, USA, 1:500), anti-Ki67
195 (#556003, BD Biosciences, USA, 1:100), anti-Tuj1 (#801201, BioLgend, USA,
196 1:500), anti-AP2α (3B5-c, DSHB, USA, 1:1000), anti-Rom1 (gift from Robert
197 Moldey, 1:10), anti-Rhodopsin (STJ95452, ST John's Laboratory, UK, 1:100),
198 anti-S-opsin (sc-14363, Santa Cruz Biotechnology, USA, 1:500), anti-M-opsin
199 (AB5405, Sigma, USA, 1:500), anti-GFP (GFP-1010, Aves labs, USA, 1:1000),
200 anti-β-catenin (#610153, BD Biosciences, USA, 1:1000), anti-N-cadherin
201 (#610920, BD Transduction Laboratories, USA, 1:500), anti-BrdU (#347580, BD
202 Biosciences, USA, 1:100), and anti-phospho-histone H3S10 (#06-570, Millipore,
203 USA, 1:2000) antibodies.
204
205 *Counting of retinal cells and synapses*
206 The cell number of each retinal cell type was counted around the area 500 μm
207 away from the optic nerve using immunostained retinal sections, and we
208 calculated the cell number per 100 μm width of retinal section. Each retinal cell
209 type was identified as follows: rod (Otx2 signal at the nuclear periphery), cone

210 (Arr3+, Otx2 signal in the soma), BC (Chx10+), horizontal cell (Calbindin+ and
211 AP2α-), AC (AP2α+), RGC (RBPMS+), and Müller glial cell (Lhx2+).
212
213 It was difficult to count the number of synapses between photoreceptor and BC
214 in 2D images of the cKO retina because the direction of the photoreceptor
215 synapse was aberrant. Thus, the number of synapses was counted using 3D
216 images reconstituted from immunostained vertical sections. The image of
217 vertical sections was acquired with a width (x-axis) of 126.8 μm, a length (y-
218 axis) of 126.8 μm, and a thickness (z-axis) of 12 μm. Then, the number of
219 synapses per 1 mm^2 of retinal surface was calculated. The regions distal to the
220 IPL were analyzed because photoreceptor synapses were not observed below
221 the IPL. Since the synapses between the rod photoreceptor and BC in the cHet
222 retina were highly dense, we counted them every 1.8 μm using 2D images and
223 integrated them. We confirmed that the number of synapses was not different
224 between 2D and 3D images.
225
226 *Processing of tissues for electron microscopy*
227 The eyeball was removed, cut in the cornea, and fixed with 2.5% glutaraldehyde
228 in PBS for 2.5 h on ice, and with 2% osmium tetroxide for 2 h. Retinas were
229 washed with 1x PBS, and dehydrated with a graded series of ethanol, followed
230 by propylene oxide, and embedded in Epon 812. Seventy-nm ultrathin sections
231 were cut by an ultramicrotome (Ultracut E; Reichert-Jung, Germany), mounted
232 on nickel grids, and stained with 2% uranyl acetate for 4 h and with nitrate for 5
233 min. Retinal sections were observed by transmission electron microscope (H-

234 7500; HITACHI Co, Japan).

235

236 *Reverse transcription real-time quantitative PCR (RT-qPCR)*

237 Total retinal RNA was isolated using Isogen II reagent (Nippon Gene, Japan)
238 following the manufacturer's instructions, and reverse transcribed into cDNA
239 using SuperScript II Reverse Transcriptase (Thermo Fisher Scientific, USA)
240 with random hexamers and oligo (dT) 12-18 primers. Diluted cDNA was used as
241 a template for qPCR using a TB Green® Premix Ex Taq™ II (Tli RNaseH Plus)
242 (Takara Bio, Japan) according to the manufacturer's instructions, on Thermal
243 Cycler Dice® Real Time System II (Takara Bio, Japan). The primer sequences
244 are listed in **Table S1**.

245

246 *Western blot analysis*

247 Retinal tissues were lysed in RIPA buffer (50 mM Tris-HCl pH7.6, 150 mM NaCl,
248 1mM EDTA, pH8.0, 1% Nonided-P40, 1% Sodium Deoxycholate, 0.1% SDS),
249 cooled for 10 min on ice, and centrifuged at 14,000 rpm for 10 min at 4ºC. Then,
250 a 3x sample buffer was added to the supernatant, and it was boiled for 10 min
251 at 95ºC. Samples were separated by SDS-PAGE and transferred to PVDF
252 membranes (Millipore, USA) using a wet transfer cell (Bio-Rad, USA). The
253 membranes were soaked in blocking buffer (5% skim milk (W/V) and 0.1%
254 Tween 20 in TBS) and incubated with anti-l-afadin antibody (1:1000) overnight
255 at 4°C or horseradish peroxidase-conjugated anti-GAPDH antibody (1:5000) for
256 2 h at room temperature. After washing with TBS/0.1% Tween-20 four times for
257 10 min each, the membranes were incubated with horseradish peroxidase-

258 conjugated anti-mouse IgG antibody for 2 h at room temperature. Signals were
259 detected using ImmunoStar LD (Fujifilm Wako, Japan).
260
261 *Antibody production*
262 cDNA fragments encoding a C-terminal portion of mouse mGluR6 (853-871
263 residues) were subcloned into *pGEX4T-1* plasmid (Amersham, UK). The GST-
264 mGluR6 fusion protein was expressed in *Escherichia coli* strain BL21 and
265 purified with glutathione Sepharose 4B (GE Healthcare, USA) according to the
266 manufacturer's instructions. The anti-mGluR6 antibody was obtained by
267 immunizing guinea pigs with the purified GST-mGluR6.
268
269 *ERG recordings*
270 Mice were dark-adapted for more than 1 h and then anesthetized deeply by
271 intraperitoneally injecting mixed anesthesia consisting of (in mg/kg) 0.3
272 medetomidine, 4 midazolam, and 5 butorphanol tartrate. We also administered
273 0.1% tropicamide and 0.1% phenylephrine to the eyes to dilate the pupil. ERGs
274 were recorded via contact lens electrodes (Mayo Corporation, Japan), and data
275 were sampled at 1,250 Hz by using the PuREC system (Mayo Corporation,
276 Japan). Reference and ground electrodes were placed in the mouth and on the
277 tail, respectively. Full-field stimulation was presented via an optical stimulator
278 equipped with white LED (RMG; Mayo Corporation, Japan), and its light
279 intensity and duration were controlled by an LED visual stimulator (LS-100;
280 Mayo Corporation, Japan). Scotopic ERGs were recorded by applying 5-ms
281 flash (1.0×10^4 cd/m^2) three times in the dark. After 10 min light adaptation

282 (31.6 cd/m^2), photopic ERGs were recorded by superimposing 5-ms flash (1.0 x
283 10^4 cd/m^2) sixteen times on the adapting background. After noise reduction by a
284 program installed in the PuREC system, ERGs were lowpass-filtered (<50 Hz)
285 on Python3 and then analyzed.
286
287 *MEA recordings*
288 The retinal preparation was made as described previously (Takeuchi et al.,
289 2018). In brief, a dark-adapted (>1 h) mouse was sacrificed by cervical
290 dislocation under a dim red light, and its eyes were enucleated. Under a
291 stereomicroscope equipped with an infrared (IR) image converter (V6833P,
292 Hamamatsu Photonics, Japan) and IR illumination (HVL-IRM, Sony, Japan), the
293 retina was isolated from the eye, and the dorsal retina was placed ganglion cell
294 layer side down onto the multielectrode array (MEA, Multichannel Systems,
295 Germany, 60pMEA200/30iR-Ti: 60 electrodes, electrode size 30x30 μm, inter-
296 electrode distance 200 μm) and attached to the MEA by suction using a vacuum
297 pump (Constant Vacuum Pump, Multichannel Systems, Germany). When
298 another type of MEA (Multi Channel Systems, Germany, 60MEA200/30iR-Ti-gr:
299 60 electrodes, electrode size 30×30 μm, inter-electrode distance 200 μm) was
300 used, a piece of anodisc (13 mm, 0.2 μm, 6809-7023, Whatman, UK) and a
301 weight with nylon fibers were placed on the retina to improve the contact with
302 MEA. Then, the MEA chamber was constantly superfused with Ames' medium
303 (A1372-25, United States Biological, USA) bubbled with 95% O_2/5% CO_2 at the
304 rate of 6.0 mL/min at 32°C. After >30 min superfusion, we started recordings.
305 Signals were amplified, sampled at 20 kHz, and stored using MEA2100-Lite-

System (Multichannel Systems, Germany). In pharmacological experiment, L-(+)-2-amino-4-phosphonobutyric acid (10 μM; L-AP4, 23052-81-5, Tocris, UK) dissolved in Ames' medium was bath-applied to the retina.

Light stimulus generated by Psychtoolbox-3 on MATLAB was presented on a monitor display (P2314H, Dell, Japan), and projected through optics on the photoreceptor layer. Flashes (24.2 or 27.3 cd/m^2, 2 s in duration, 1,600 μm in diameter) were presented seven times every 8 s. In some experiments, the retina was stimulated by 5-ms diffuse green LED light (2.5 x 10^4 photons/s/μm^2 for mERG recordings, 4.8 x 10^3 photons/s/μm^2 for rod stimulation: LED; λ_{max} = 518 nm, IF filter; 510 nm, FWHM 10 nm, #65-697, ND filter; OD 1.0 #47-207, Edmund Optics, USA) or 5-ms diffuse UV LED light (3.3 x 10^4 photons/s/μm^2 for cone stimulation; LED; λ_{max} = 370 nm, KED365UH, IF filter; 360 nm, FWHM 10 nm #67-827, Edmund Optics, USA) controlled by a function generator (WF1973, NF Corporation, Japan) three times every >10 s.

Spike sorting

For spike sorting, the algorithm described on Python3 was used. The data were high pass-filtered (>300 Hz), and minimum values were detected by using scipy.signal.argrelmin function. To decide whether each detected minimum value reflects the peak of spike event, we used a threshold value defined by the following formula (Quiroga et al., 2004).

$$threshold = -4 \times median\ (|x|\ /0.6745),$$

where x represents each data point, *as* our data were recorded extracellularly,

the threshold polarity was reversed. The detected values (> threshold) were judged as spike events, and the waveform of spikes was obtained from the data points between -1 and +2 ms from each peak. The 1st and 2nd differences (numpy.diff) of each waveform were joined, and then principal component analysis (PCA) was carried out for feature compression to two dimensions. Then, clustering was performed using template matching method (Zhang et al., 2004) and Uniform Manifold Approximation and Projection (UMAP). To check the accuracy of spike sorting, we performed autocorrelation analysis to confirm the presence of a refractory period (the number of spike events at ± 1 ms bin was less than 1% of total spike events).

Classification of RGCs based on PSTH

Using the MEA system, we recorded firing responses of RGCs to light stimulation (0.24 or 0.27 cd/m^2 in intensity, 2 s in duration) presented 7 times from the monitor and calculated the peristimulus time histograms (PSTHs) with 20-ms bin. The PSTH was smoothed by a Gaussian filter (kernel size: 3 bins, $\sigma = 1$). The light-evoked response was defined when the firing rate of the PSTH exceeded the threshold (increment >+4 SDs, decrement <-2 SDs) determined by the spontaneous firing rate for 2 s before light stimulation. RGCs were classified into “ON” (increment within 2 s after light onset), “ON-OFF” (increment within 2 s after light onset and offset), “ON-OFF inhibition” (decrement within 2 s after light onset and offset), “OFF” (decrement within 2 s after light onset and/or increment within 2 s after light offset), and “None” (no clear change in firing rate) types.

To determine the type of photoreceptor inputs, a 2-s flash of green LED (λ_{max} = 510 nm, 4.8×10^3 photons/s/μm^2) and 2-s flash of UV LED (λ_{max} = 360 nm, 3.3×10^4 photons/s/μm^2) were applied seven times at 8-s interval serially. We classified RGCs into “Rod (+)” (responded to green LED), “Cone (+)-Rod (+)” (responded to both green and UV LEDs), “Cone (+)” (responded to UV LED), and “None” responsive types.

Receptive Field

The reverse correlation method was used to detect the receptive field (RF). Pseudorandom checkerboard patterns (32×32 pixels; black/white = 1; pixel size 50×50 μm) were applied to the retina at 60 Hz. The checkerboard images that preceded each spike event (20 frames) were averaged (spike-triggered average: STA). The intensity of each pixel was +1 or 0, and thus the area with pixels that exceeded +5 SDs of the noise intensity (~0.5: the SD calculated from the frame at t = 0) were judged to be an RF, and the pixel with maximal intensity was defined as the RF center. An ellipse was fitted to the area, and its long and short axes, as well as the area, were calculated. To estimate the temporal profile of RF, the mean intensity of 5×5 pixels in the RF central region was obtained from a series of averaged frames. The temporal profile of RF was normalized, assuming that the mean of the frame at t = 0 was 0. The normalized temporal profiles were compressed into two dimensions by using UMAP, and then k-means clustering was performed.

Visual behavioral tests

We examined the visual behavior of the afadin cHet, afadin cKO, and ONC (optic nerve crush) mice. The optic nerve crush was performed as previously described (Cameron et al., 2020), and successful nerve damage was confirmed by absence of a pupillary light reflex.

The optomotor response (OMR) test was performed as described previously with slight modifications (Kretschmer et al., 2015, 2013; Warwick et al., 2024). Mice were placed on a central platform surrounded on all four sides by monitors, with a mirror positioned on the floor beneath the platform. Stimuli were comprised of vertical square wave gratings (white; 116.2 cd/m^2, black; 1.66 cd/m^2, Michelson contrast; 97.2) with spatial frequency (0.056, 0.10, or 0.27 cycles/degree) manipulated to induce the illusion of a virtual cylinder with identical spatial frequency across the entire display at a constant speed of 12 degree/second. Each trial consisted of 2 min of drifting gratings, followed by either 30 s or 2 min of a uniform white screen (88.6 cd/m^2), and then another 2 min of drifting gratings in the opposite direction. This trial was repeated three or four times. Head movements were tracked using a camera (29.97 fps, AN-S093, KEIYO, Japan) and the number of head movements consistent with the stimulus direction and speed was counted in a blind manner.

For the visual cliff test, mice were placed along the centerline of a transparent plane (60x60 cm, width x length), positioned 80 cm high above the floor. The half of the arena was immediately beneath the platform covered by a black-and-

white checkered sheet (pixel size; 2x2 cm) (shallow side) and the other half was a transparent plane, below which the identical checkerboard pattern was located on the floor (deep side). Mouse behavior was recorded using the camera, and the percentage of time spent on each side during the first 5 minutes was calculated by an observer in a blind manner.

Statistical Analysis

In Figures 2H-L, 3E and 3F, a generalized linear mixed model (GLMM) was used. In Figures 2F, 2G, 9D, and 9F, a log1p-transformation followed by a linear mixed model (LMM) was applied. In Figures 2M, S4A-C, S4E, and 9B, Student's t-test was used. In Figure 8C and 8D, Dunn's test was used. In Figure 8F, the one-way ANOVA followed by Tukey's multiple comparisons test was applied. In Figure S3C, LMM was used. In Figures 5C-F and 7D, the Mann-Whitney U test was used. In Figure 6A, the Kolmogorov-Smirnov test was used. In Figures S4D, S4F, and S6B–D, in which multiple stages and genes were analyzed, and data distribution and variance differed across conditions. Statistical tests (Student's t-test, Welch's t-test, or Mann–Whitney U test) were chosen accordingly. The specific statistical test used for each stage or gene is described in the corresponding Figure legends. Error bars denote standard error. The following asterisks in Figures indicate *p* values: * <0.05, ** <0.01, *** <0.001.

426 **RESULTS**

427 **Afadin is localized to adherens junctions, synaptic regions, and the**
428 **surface of bipolar cells in the retina**

429 To elucidate afadin localization in mature retina (1-month-old: 1M), we
430 immunostained retinal sections with anti-afadin antibody. Afadin signals were
431 observed in the outer segment (OS), outer limiting membrane (OLM), outer
432 plexiform layer (OPL), inner nuclear layer (INL), and inner plexiform layer (IPL)
433 (Figure 1A *Top*). These signals were not observed in retinal sections
434 immunostained using anti-afadin antibody pre-absorbed with the antigen
435 peptide (Figure 1A *Bottom*). Thus, we confirmed that the signals are specific to
436 afadin. To explore whether afadin is co-localized with nectin in the retina, we
437 analyzed afadin and nectin localization in the retina by immunostaining using
438 antibodies against afadin and nectins1-3. Afadin signals were aligned and
439 overlapped with all three nectin signals in the OLM (Figures 1B, C, S1A),
440 consistent with the previous finding that AJs are formed in the OLM in the retina
441 (Willbold and Layer, 1998). Nectin-1, unlike nectin-2 and nectin-3, was partially
442 co-localized with afadin at the OPL and IPL, in addition to the OLM (Figures 1B,
443 S1B). Nectin-1 was co-localized with afadin in cone synapses immunostained
444 with Arrestin3 (Arr3, cone photoreceptor marker), suggesting that puncta
445 adherent junctions may be formed between cone pedicles and BC dendritic tips.
446 In the retina at postnatal day 0 (P0), afadin and nectin-1 signals were observed
447 in the outer retinal surface where AJs are formed (Figure S1C) (Koike et al.,
448 2005). Immunostaining with anti-afadin, anti-SCGN (Type 2-6 cone BC marker)
449 (Puthussery et al., 2010), and anti-PKCα (rod BC marker) revealed that afadin

450 localizes to the dendritic tips, cell bodies, and axons of ON- BCs and at least
451 cell bodies of OFF-BCs (Figure 1D).
452
453 **Afadin is required for proper retinal lamination**
454 To investigate the role of afadin in the retina, we generated retina-specific *afadin*
455 cKO mice by crossing *afadin flox* mice with *Dkk3-Cre* mice (Majima et al., 2009;
456 Sato et al., 2007; Yamamoto et al., 2020). Cre activity in *Dkk3-Cre* mice was
457 confirmed by crossing with *R26R-H2B-EGFP* reporter mice (Abe et al., 2011), in
458 which Cre-dependent excision of a *loxP*-flanked STOP cassette drives nuclear
459 EGFP expression from the *Rosa26* locus (Figure S2A, B). Afadin was not
460 detected at the protein level by Western blotting in the *afadin* cKO retina (Figure
461 S2C). The *afadin* cKO mouse was viable and showed no gross morphological
462 abnormalities. To examine retinal lamination and morphology, using the cKO
463 retina at 1M, we performed toluidine blue staining. We found that there were no
464 clear outer and inner segments of photoreceptors in the outer retina, no distinct
465 OPL, and no clear compartmentalization of the ONL and INL (Figure 2A). Rod
466 photoreceptors, identified by inverted nuclear architecture (Solovei et al., 2009)
467 (Figure 2A insets), were widely scattered in the cKO retina, whereas the IPL and
468 GCL appeared intact. Furthermore, rosette-like structures, which lacked cell
469 bodies centrally, were sometimes observed in the cKO outer retina (Figure 2A,
470 B, C: arrowhead).
471
472 To investigate the defects in the OS of the cKO retina in more detail, we stained
473 retinal sections with rhodamine-labeled peanut agglutinin (PNA, a marker of

474 cone photoreceptor outer segment and axon terminals) or antibodies against
475 Rom1 (rod OS marker), Rhodopsin (rod OS marker), S-opsin (S-cone OS
476 marker), and M-opsin (M-cone OS marker). Rhodopsin, Rom1, S-opsin, and M-
477 opsin play central roles in phototransduction in the OS (Clarke et al., 2000;
478 Greenwald et al., 2014; Tanimoto et al., 2015; Xu et al., 2020). Distribution of
479 Rom1, Rhodopsin, S-opsin, M-opsin, and PNA signals in the cKO retina differed
480 significantly from those of the a*fadin* cHet retina. In the cKO retina, Rom1,
481 Rhodopsin, S-opsin, M-opsin, and PNA signals were remarkably decreased in
482 number and mislocalized in the retina (Figure 2B, C). These markers were not
483 observed in the rosette-like structure of the cKO retina, suggesting that the
484 rosette-like structure is different from the photoreceptor rosette as reported
485 (Stuck et al., 2012). Electron microscopic analysis also demonstrated that only
486 a few OS structures were observed between retinal cells in the disrupted ONL
487 and INL regions of the cKO retina (Figure S2D). These findings indicate that rod
488 and cone phototransduction may be severely impaired in the cKO retina. To
489 investigate the distribution of cone and rod photoreceptors in the cKO retina, we
490 performed wholemount immunostaining with antibodies against Arr3,
491 Rhodopsin, and Rom1. Cell bodies of cone photoreceptors were arranged
492 regularly in the cHet retina, whereas cone photoreceptor arrangements and
493 morphology were significantly disordered in the cKO retina (Figure 2D). Rom1,
494 Rhodopsin, and Arr3 signals were decreased but relatively dense in some areas
495 (Figure 2D). These results suggest that photoreceptor distribution is disrupted,
496 but photoreceptors remain in some areas heterogeneously.
497

498 We further investigated AJs in the cKO retina by immunostaining with OLM
499 adherens junction markers β-catenin, N-cadherin, and nectin-1. We found that
500 these signals were scattered in the cKO retina (Figure S2E). This data suggests
501 that AJs in the OLM are disrupted in mature cKO retina.
502
503 As toluidine blue staining of the cKO retina suggested mislocalization of each
504 cell type, we investigated the position of each retinal cell body in the cKO retina
505 by immunostaining with retinal cell type-specific markers; Otx2 (a photoreceptor
506 and BC marker), Chx10 (a BC marker), Arr3, Calbindin (a horizontal cell and AC
507 marker), AP2α (an AC maker), RBPMS (a RGC marker), and Lhx2 (a Müller
508 glial cell marker) (Figure 2E). All retinal cell types were aligned in restricted and
509 orderly regions in the cHet retina. In the cKO retina, the spatial organization of
510 rod photoreceptors, BCs, cone photoreceptors, horizontal cells, and Müller glial
511 cells appeared particularly disrupted, whereas positions of ACs and RGCs
512 remained relatively intact, except for the immediately surrounding region of
513 rosette-like structures. To quantitatively assess the retinal cell positioning in the
514 cKO retina, the distance from the soma of each cell type to the outer or inner
515 retinal surface was measured (Figure 2F-L). The distance for each cell type in
516 the cKO retina was significantly different from that in the cHet retina. In the cKO
517 retina, BCs, horizontal cells, Müller glial cells were positioned close to the outer
518 retinal surface and ACs were close to the inner retinal surface, whereas
519 photoreceptors and RGCs were positioned away from the outer and inner
520 retinal surfaces, respectively.
521

522 Notably, BCs in the cKO retina were broadly distributed throughout the retina
523 (Figure 2H). Rod photoreceptors also tended to be dispersed throughout the
524 cKO retina. However, approximately 75% of them in the cKO retina were
525 located within 60 μm of the outer retinal surface, which corresponds to the
526 region where all rods are positioned in the cHet retina (Figure 2G). Cone
527 photoreceptors, horizontal cells, and Müller glial cells were similarly spread, but
528 their distribution was largely confined to the area distal to the IPL (Figure 2F, I,
529 J). Although ACs and RGCs were mainly located in the inner retina, a sparse
530 distribution was also observed throughout the retina, which may be attributed to
531 the cells surrounding the rosette-like structure (Figure 2K, L). The reduction in
532 the distance from ACs to the inner retinal surface in the cKO retina is
533 conceivably due to a shortening of the IPL (Figure 2K), though there was no
534 significant difference in retinal thickness between cHet and cKO retinas (Figure
535 2M). The cKO mice appeared to show greater inter-individual variability in
536 retinal layer structure and cell positioning than the cHet mice.
537
538 Immunostaining with an anti-GS antibody (a Müller glial cell marker) showed
539 that Müller glial cell morphology was affected, especially at the distal part.
540 However, a distinct inner limiting membrane was retained in the cKO retina
541 (Figure S2F). It has been reported that defects in the distal processes of Müller
542 glia are associated with abnormal retinal vasculature (Shen et al., 2012). Thus,
543 we immunostained the cKO retina with anti-CD31, a blood vessel marker, but
544 no apparent vascular abnormalities were detected (Figure S2G). These results
545 indicate that afadin is essential for normal retinal lamination.

546

547 **Ablation of afadin results in the remarkable decrease and mislocalization**
548 **of photoreceptor-BC synapses**

549 No distinct OPL structure in the cKO retina suggests that synapses between
550 photoreceptor and BC may be disrupted. To assess their integrity, we
551 immunostained retinal sections of the cKO mouse (1 M) with antibodies against
552 Bassoon (a photoreceptor synaptic ribbon marker), PSD95 (a photoreceptor
553 synaptic terminal marker), mGluR6 (an ON-BC dendritic tip marker), GluR5 (an
554 OFF-BC dendritic tip marker), PKCα, and PKARIIβ (a type 3b OFF cone BC
555 marker). In the cHet retina, photoreceptor synapses containing synaptic ribbons
556 formed a row in the OPL (Figures 3A, B, S3A). On the other hand, in the cKO
557 retina, the row of photoreceptor synapses was not observed, and
558 photoreceptor-BC synapses were remarkably reduced in number. Bassoon and
559 mGluR6 were aberrantly distributed, and the position of the soma and dendritic
560 tips of rod BCs was noticeably disturbed (Figure 3A). Only a few ribbon
561 synapses remained (Figure 3A arrowheads). The 3D reconstructions of the
562 confocal image stacks showed more clearly that photoreceptor synapses
563 decreased in number and mislocated in the cKO retina (Figure 3C, D). The
564 contact between the axon terminal of photoreceptors and the dendrite of ON-
565 and OFF-BCs was also significantly reduced in number, suggesting that
566 photoreceptor-BC synapses were considerably lost in the cKO retina (Figures
567 3B, D, S3A, B). Along with these defects, GluR5 signals with a branch-like
568 pattern were detected in the IPL of the cKO retina, though no GluR5 signals
569 were found in the IPL of the cHet retina (Figure 3B, D). Photoreceptor-ON BC

570 ribbon synapses and photoreceptor-OFF BC synapses in the outer retinal
571 region beneath 1 mm^2 of the surface area of the cKO retina were significantly
572 reduced to about 5% and 15% of those in the cHet retina, respectively (Figures
573 3E, F, S3C). These results indicate that afadin may regulate the formation and
574 localization of photoreceptor synapses.
575
576 **Afadin is required for proper localization of GluR5 to OFF BC dendrites**
577 GluR5, a kainate receptor subunit that forms functional homomeric and
578 heteromeric channels, is specifically expressed in OFF BCs and localizes to
579 their dendrites (Haverkamp et al., 2003). To investigate GluR5 localization in
580 more detail, we immunostained the cKO retina with anti-GluR5, anti-SCGN, and
581 anti-PKCα antibodies. We found that ectopic GluR5 signals in the IPL
582 overlapped not only with SCGN but also PKCα in the cKO retina (Figure 4A).
583 These data indicate that afadin may be required for specific localization of
584 GluR5 in OFF BC dendrites. It seems likely that ectopically localized GluR5 may
585 receive glutamate released from surrounding cells in the IPL, resulting in
586 depolarization of ON- and OFF-BCs. It should be noted that there were no
587 remarkable differences between cKO and cHet retinas in the localization of
588 glutamate transporter EAAT5 and vesicular glutamate transporter vGlut1 to the
589 axon terminal of photoreceptors and BCs (Figures 4B, S3D, E). It has been
590 reported that mGluR6 localization to ON BC dendritic tips requires trans-
591 synaptic interaction with ELFN1 in the synaptic cleft and that ELFN1 ablation
592 results in a remarkable reduction of mGluR6 in ON BC dendritic tips (Cao et al.,
593 2015). As GluR5 localization may also be regulated by trans-synaptic interaction

594 with photoreceptor synaptic terminal proteins, it seems possible that the defect
595 of photoreceptor-OFF BC contacts prevents this trans-synaptic interaction,
596 resulting in GluR5 mislocalization in the cKO retina.
597
598 Then, we investigated the IPL structure in the cKO retina by immunostaining it
599 with anti-ChAT, Calbindin, and Calretinin antibodies. Distinct ON- and OFF
600 ChAT bands, Calbindin bands, and Calretinin bands were observed in the cKO
601 retina (Figure S3F). However, type 2-6 BCs immunostained with SCGN were
602 slightly disturbed in the axon terminal position (Figures 4A, B, S3D). These
603 results suggest that stratification patterns in the IPL may be slightly impaired but
604 almost intact in the cKO retina. Immunostaining analysis with anti-HPC-1 (also
605 known as syntaxin, an AC marker), anti-Calbindin, anti-RBPMS, and anti-Tuj1
606 (an RGC marker) antibodies revealed that the rosette-like structure contains AC
607 and RGC processes inside (Figure 4C). These data indicate that the rosette-like
608 structure in the cKO may be an ectopic IPL, termed “acellular patches” (Nahar
609 and Cho, 2022).
610
611 **Retinal cell fate is altered in the cKO retina**
612 To examine whether afadin loss affects retinal cell fate determination, we
613 counted the number of retinal cells immunostained with each retinal cell marker.
614 In the cKO retina at 1M, BCs significantly increased to about 150% of the cHet
615 retina, but rods, cones, and Müller glial cells were significantly decreased to
616 about 30%, 40%, and 80% of the cHet retina, respectively (Figure 4D). PKCα-
617 positive cells and SCGN-positive cells were significantly increased (Figure

618 S4A), indicating that both rod- and OFF-BCs were increased in the cKO retina.
619 In contrast, the number of rod BC processes in the IPL was significantly
620 decreased in the cKO retina (Figure S4B). These data suggest that ectopically
621 located BCs may increase in the cKO retina at 1M. A significant increase in BCs
622 and a significant decrease in photoreceptors were also observed in the cKO
623 retina at P14, a stage at which retinal differentiation is complete (Figure S4C).
624 Consistently, the expression of marker genes for photoreceptors and BCs was
625 significantly decreased and increased, respectively, in the cKO retina (Figure
626 S4D). In contrast, the number of Müller glial cells was unaltered in the cKO
627 retina at P14 (Figure S4C), suggesting that the reduction in Müller cells
628 observed at 1M may result from cell death after P14 rather than a differentiation
629 defect. To assess whether retinal cell fate changes occur during differentiation,
630 we examined the number of BCs and the expression of rod marker genes in the
631 cKO and cHet retinas at P1, P3, and P5. No significant differences were
632 observed between genotypes at P1 and P3, whereas the number of BCs was
633 significantly increased, and the expression of rod marker genes was
634 significantly decreased in the cKO retina at P5 (Figure S4E, F). These results
635 suggest that defects in cell fate determination of BCs and rod photoreceptors
636 begin to emerge between P3 and P5. Based on these data and ectopic
637 localization of GluR5 to ON-BCs in the cKO retina (Figure 4A), we propose that
638 afadin may be required for normal retinal cell fate determination and gene
639 expression.
640
641 **Retinal structure is severely disrupted during development in *afadin* cKO**

642 **mice**

643 To investigate whether the aberrant lamination in the cKO retina can be
644 attributed to a defect in development or maintenance, we immunostained the
645 developing cHet and cKO retinas using markers for individual retinal cell types,
646 outer segments, and photoreceptor synapses (Figures 4E, S5A-D). In the cKO
647 retina at P1, retinal cells appeared to be organized into distinct multicellular
648 compartments with apparent boundaries (Figures 4E, S5A, B). RGCs, ACs, and
649 their dendritic processes, which are components of the IPL, were localized
650 along the boundaries of these compartments (Figure S5A, B). Furthermore,
651 RGCs and ACs were observed in the outer part of the retina. At P3 and P5, the
652 interspaces between compartments appeared to be reduced, coinciding with an
653 increase in RGCs and ACs positioned on the inner side of the retina (Figure
654 S5A, B). By comparison, the positioning of BCs and rod photoreceptors appears
655 to remain disorganized throughout postnatal development (Figure 4E). Contrary
656 to our expectation that retinal structure would become increasingly disorganized
657 as development progresses, laminar disruption in the cKO retina appeared
658 more severe at earlier postnatal stages than at later ones, particularly in the
659 IPL, ACs, and RGCs (Figure S5A, B). Aberrant acellular regions were observed
660 in the cKO retina from P1 through P14 (Figures 4E, S5A-C). Some of these
661 regions contained AC processes and were surrounded by AC and RGC somata
662 from P3 onward (Figure S5A, B). Correspondingly, clear signals of rod outer
663 segment markers were observed in the interior of some acellular regions at P8,
664 P11, and P14 (Figure S5C). At 1M, these structures were not observed in the
665 cKO retina (Figure 2B). These data suggest that both acellular patch and

666 photoreceptor rosette may be formed in the developing retina, but
667 photoreceptor rosette may degenerate after P14. The outer segment marker
668 signals were disorganized in the cKO retina at P8, P11, and P14 (Figure S5C).
669 Moreover, the row of rod and cone photoreceptor synapses was not observed in
670 the cKO retina at P11 (Figure S5D). These data indicate that proper
671 development of retinal lamination and synapse formation is impaired in the cKO
672 retina.
673
674 **Small local field potentials are recorded from the cKO retina**
675 To examine whether the cKO mouse retina can respond to light stimulation, we
676 first recorded electoretinogram (ERG) from anaesthetized animals. Under the
677 scotopic condition, a flashlight was applied to eyes in the dark (Figure 5A *left*).
678 Scotopic ERG from the cHet mouse showed a negative a-wave and a following
679 positive b-wave, whereas both waves from the cKO mouse were almost flat.
680 Under the photopic condition, the mouse was adapted to the background light
681 for 10 min, then a flashlight was superimposed on the adapting background
682 (Figure 5A *right*). Photopic ERGs from the cHet mouse showed a small a-wave
683 and a prominent b-wave, whereas those from the cKO mouse were almost flat.
684 These results may be attributed to the scattered distribution of rod and cone
685 photoreceptors, a lack of a uniform photoreceptor layer, and the decrease of
686 outer segments and photoreceptor synapses in the cKO retina (see Figures 2
687 and 3).
688
689 Then, to examine whether local field potentials can be detected from the cKO

690 retina, we performed MEA recordings from the retinas isolated from the cKO
691 and cHet mice. Surprisingly, a flashlight could occasionally evoke micro-ERGs
692 (mERGs) from the cKO retina (SD of the amplitude during 300 ms after the
693 flashlight onset; >50 μV, 13/590 electrodes, n = 10 retinas from 6 mice) (Figure
694 5B *right*). However, the amplitude of mERGs from the cKO retina was smaller
695 than that from the cHet retina (SD of the amplitude during 200 ms after the
696 flashlight onset; >1,000 μV, 292/413 electrodes, n = 7 retinas from 4 mice)
697 (Figure 5B *left*). As the a-wave represents hyperpolarization of the
698 photoreceptors and the b-wave arises from the inner retina, predominantly from
699 ON BCs with a contribution from Müller glial cells (Perlman, 2020), the first
700 negative and following positive waves of mERGs may correspond to the a- and
701 b-waves, respectively. To confirm this, L-AP4, an agonist of mGluR6, was bath-
702 applied to suppress the response of ON BCs. In the presence of L-AP4, the
703 second positive wave disappeared, whereas the first negative wave was
704 enhanced in the cHet retina and remained in the cKO retina (Figure 5B),
705 indicating that the first negative and following positive waves are the a- and b-
706 waves, respectively. We compared the amplitude and implicit time (time-to-peak
707 latency) of the a- and b-waves and found that both a- and b-waves were
708 significantly smaller in amplitude (Figure 5C) and longer in implicit time in the
709 cKO retina than those in the cHet retina (Figure 5E). The ratio of b-wave
710 amplitude to a-wave amplitude (b/a) was significantly smaller in the cKO retina
711 than in the cHet retina (Figure 5D), suggesting that the efficiency of synaptic
712 transmission from photoreceptors to ON BCs may be decreased in the cKO
713 retina. However, the difference of the implicit time between a- and b-waves was

714 similar in the cKO and cHet retinas (Figure 5F), suggesting that signals from
715 photoreceptors to ON BCs may be transmitted properly. These results indicate
716 that despite severe disorganization of the cKO outer retina, photoreceptors can
717 still respond to light stimulation and that the synaptic transmission from
718 photoreceptors to ON-BCs remains functional.
719

720 **RGCs in the cKO retina evoke firings to light stimulation**

721 Using the MEA system, we recorded spike discharges from RGCs in retinas
722 isolated from the cKO and cHet mice. The frequency of spontaneous firings in
723 the dark was not different significantly between cKO and cHet retinas (cHet;
724 12.5 ± 19.2 Hz, n = 434, cKO; 10.8 ± 14.6 Hz, n = 388, p = 0.79, Mann-Whitney
725 U test). We examined whether RGCs in the cKO retina respond to light
726 stimulation. The isolated retina was stimulated by a flash seven times every 8 s,
727 and the PSTH was calculated for each RGC after spike sorting. RGCs could be
728 classified into “ON”, “ON-OFF”, “ON-OFF inhibition”, “OFF”, and “None” types
729 (Figure 6A, B; see **MATERIALS and METHODS**). All types were found in both
730 cKO and cHet retinas, and the composition of RGC types was similar in both
731 retinas (Figure 6C). We also investigated whether RGCs received both rod and
732 cone inputs and found that > 60% of RGCs among successfully spike sorted
733 RGCs in both the cKO and cHet retinas received both inputs (Figure 6D).
734

735 **Receptive fields are characterized in some RGCs**

736 Using pseudorandom checkerboard pattern stimulation, we examined the
737 properties of spatiotemporal RF of RGCs by calculating the spike-triggered

average. We could identify RFs in the cKO retina. To check the morphology of the retina where RFs were identified, the retina was removed from the MEA after recording, and sliced retinal sections were immunostained with anti-PKARIIβ, anti-PSD95, and anti-PKCα antibodies (Figure 7A). The sectioned region clearly showed impairment of the outer retina, where it was difficult to identify or locate photoreceptors. On the other hand, the inner retina was apparently normal, and both the IPL and the proximal part of the INL could be recognized. Even though the outer retina was severely impaired, we could identify RF of RGCs (Figure 7B). However, the cells with clear RF were fewer in the cKO retina (69/388 cells, n = 4 retinas) than those in the cHet retina (195/434 cells, n = 4 retinas). By fitting ellipse to each RF, we measured the short and long axes and calculated the RF area (Figure 7C, D, E). The RF area in the cKO retina was significantly smaller than that in the cHet retina. We tried to find an antagonistic surround of RFs, but it was difficult to detect a clear surround in both cKO and cHet retinas.

The temporal profile of RFs was calculated, and the principal component analysis was performed. Then, using UMAP for clustering, we could recognize 5 clusters (Figure 7F, cKO; n = 4 retinas, cHet; n = 4 retinas). The temporal profile belonged to each cluster was superimposed separately (Figure 7G). Among 5 clusters, clusters 1 and 2 did not include the temporal profiles calculated from RGCs in the cKO retina. The temporal profiles of cluster 1 and cluster 2 were ON and OFF types, respectively, each of which had a shorter time-to-peak latency than the other temporal profiles obtained from RGCs in both cKO and

762 cHet retinas (Figure 7H). These results indicate that the light-evoked responses
763 of RGCs in the cKO retina are not as refined as cHet. Actually, the rising time of
764 transient responses (determined by an upward deflection soon after light
765 stimulation obtained from the cumulative curve of each PSTH) was significantly
766 longer in the cKO retina (58.5 ± 19.8 ms, n = 17) than in the cHet retina (43.0 ±
767 17.8 ms, n = 23) (***$p < 0.001$, Student's test).
768
769 It has been reported that degenerated retinas, such as the *rd1* retinas (Poria
770 and Dhingra, 2015), show oscillatory spontaneous firings in RGCs. Thus, we
771 checked whether RGCs in the cKO retina show RGC oscillations. RGCs in the
772 cKO retina showed oscillations (P30; 1.55% of 382 RGCs, 14.0 ± 2.4 Hz, n = 4
773 retinas, P40; 15.0% of 333 RGCs, 9.2 ± 3.8 Hz, n = 4 retinas). On the other
774 hand, RCGs in the cHet retina did not show obvious RGC oscillations (0% of
775 432 RGCs, n = 4 retinas).
776
777
778 **Afadin cKO mice retain partial visual function**
779 As the MEA analyses suggested partial preservation of retinal functions in the
780 cKO retina, we further examined whether cKO mice retained visual function,
781 using visual behavior tests. We first conducted the optomotor response (OMR)
782 test, a robust method for assessing contrast-based visual function and
783 estimating visual acuity in mice (Thaung et al., 2002; Ye et al., 2021). The OMR
784 test measures head-tracking movements in response to a vertical square wave
785 grating stimulus (Figure 8A). Mice capable of detecting contrasting motion

786 passing through their visual field exhibit head-tracking movements in response
787 to stimuli (Kretschmer et al., 2015; Mitchiner et al., 1976; Schmucker et al.,
788 2005). Apparent head-tracking movements were observed in the cHet and cKO
789 mice during presentation of drifting grating stimuli at spatial frequencies of 0.056
790 and 0.1 cycles/degree, but not in those with optic nerve crush (ONC), in which
791 the optic nerve had been mechanically crushed, resulting in vision loss (Figure
792 8B, C). The number of head-tracking movements in response to these stimuli
793 was significantly higher in the cHet and cKO mice than in the ONC mice. At 0.27
794 cycles/degree, the cKO mice hardly exhibited head-tracking movements, in
795 contrast to the cHet mice, and no significant difference was observed between
796 the cKO and ONC mice under this condition. The number of movements was
797 significantly lower in the cKO mice than in the cHet mice at all three spatial
798 frequencies (Figure 8C). There was no significant difference in the number of
799 head-tracking movements across the three spatial frequencies in the cHet mice,
800 whereas in the cKO mice, the number tended to decrease with increasing
801 spatial frequency (Figure 8D). These data suggest that the cKO mice can
802 recognize moving visual stimuli, but their ability is inferior to that of the cHet
803 mice.
804
805 We further conducted the visual cliff test to evaluate visual performance in a
806 perceptual task. This test exploits rodents' innate tendency to avoid the deep
807 side of the cliff—a plexiglass surface suspended 80 cm above a checkerboard
808 on the floor—and prefer the shallow side, where the plexiglass covered directly
809 atop the checkerboard (Figure 8E) (Fox, 1965). The cHet mice spent

810 approximately 80% of their time on the shallow side, significantly more time
811 than the cKO and ONC mice, while the cKO mice did not differ significantly from
812 the ONC mice in time spent on the shallow side (Figure 8F). Nonetheless, some
813 cKO mice exhibited a behavior in which they looked down toward the bottom of
814 the deep side and quickly backed away (Video 1). This behavior, observed in
815 the cHet mice but not in the ONC mice, may imply that they can visually
816 recognize the deep side (Video 2). Furthermore, the cKO mice, but not the ONC
817 mice, showed a significant preference for the shallow side over the deep side
818 (57.35%, $p = 0.048$, one-sample t-test, figure not shown). These results indicate
819 that visual information from the retina is transmitted to the brain and visual
820 function is partially maintained in *afadin* cKO mice.
821
822 **Ectopic AJs and aberrant localization of progenitor cells are observed in**
823 **the developing *afadin* cKO retina**
824 As RGC oscillations were observed in the cKO retina, like the *rd1* retinas with
825 photoreceptor degeneration (Choi et al., 2014), we examined whether RGC
826 oscillations were related to cell death in the cKO retina. Using anti-active
827 caspase3 (an apoptotic cell marker), we counted the number of dead cells
828 immunohistochemically. We found that dead cells were significantly increased in
829 the cKO retina at around P30 (Figure S6A, B). These findings suggest that the
830 progressive cell death observed in the cKO retina may lead to a further
831 decrease of photoreceptors, resulting in an increase of oscillatory RGCs at P40.
832 Apoptotic cells were significantly increased in the cKO retina in the developing
833 stage at P1, P3, P5, and P14 (Figure S6B). In the cKO retina at 1 M, the

834 number of rod photoreceptors and Müller glial cells was significantly reduced to
835 approximately 60% and 70% of that at P14, respectively (P14; rod 98.3 ± 3.8,
836 Müller glial cell 17.2 ± 3.3, n = 3, 1M; rod 57.3 ± 17.3, Müller glial cell 12.4 ± 1.5,
837 n = 4. rod p = 0.011, Müller glial cell p = 0.046 by Student's t-test), in contrast to
838 the cHet retina, in which the number of rod photoreceptors remained
839 unchanged (P14; rod 176.5± 14.3, Müller glial cell 17.3 ± 1.4, n = 4, 1M; rod
840 185.9 ± 17.5, Müller glial cell 15.7 ± 2.3, n = 4, rod p = 0.43, Müller glial cell p =
841 0.27 by Student's t-test). This reduction may result from ongoing rod cell death
842 even after the completion of differentiation.
843
844 Then we investigated the mechanism underlying lamination defects in the cKO
845 retina. We previously demonstrated that the photoreceptor-cell specific *aPKCλ*
846 KO retina shows disruption of AJs and mislocalization of mitotic progenitors in
847 developing stage, followed by severe lamination defects in adults (Koike et al.,
848 2005). In the developing retina, AJs are observed in the outer retinal surface,
849 where progenitor cells divide and migrate toward the inner retina. To investigate
850 the possibility that disruption of AJs may lead to abnormal cell migration and
851 lamination, we immunostained the cKO retina at P0 with anti-β-catenin, N-
852 cadherin, nectin-1, and phospho-histone H3S10 (pHH3, a marker of the mitotic
853 cell) (Figure 9A). N-cadherin, nectin-1, and β-catenin signals were obviously
854 detected, but these signals were localized in the inner retina with aberrant
855 patterns. These signals were slightly observed in the outer retina. These data
856 indicate that ectopic AJs are present in the cKO retina. Mitotic cells
857 immunostained by pHH3 were localized near the ectopic AJs. The number of

858 pHH3-positive cells was significantly increased to approximately 150% of that in
859 the cHet (Figure 9B). At P1, P3, and P5, mitotic cells were also mislocalized to
860 the middle retinal region in the cKO mice, and their distance from the outer
861 retinal surface was significantly larger —approximately 45 μm, 70μm, and
862 75 μm, respectively— than that in the cHet (Figure 9C, D). Mitotic cells showed
863 a broader distribution in the cKO retina than in the cHet. We further examined
864 the distribution of retinal progenitor cells during development. In the cHet retina,
865 progenitor cells labeled with BrdU were scattered but relatively enriched in the
866 middle region at P1 (Figure 9E, F). As the development progressed, the number
867 of progenitor cells decreased, and their distribution was progressively confined
868 to the middle region of the retina. In the cKO retina, progenitor cells were more
869 broadly distributed (Figure 9E, F). At P5, no significant difference in the distance
870 was observed between the cHet and cKO retinas However, progenitor cells in
871 the cKO retina showed a trend toward a broader distribution compared to the
872 cHet retina. Retinal thickness and the number of progenitor cells did not differ
873 significantly between the cHet and cKO retinas at P1, P3, and P5 (Figure S6C,
874 D). These data suggest that progenitor cells may divide at ectopic regions and
875 migrate aberrantly into the cKO retina, resulting in lamination defects.
876
877

878 **DISCUSSION**

879 In the current study, we showed that the *afadin* cKO retina exhibits various
880 severe pathological defects, including photoreceptor morphological defects,
881 mislocalization, reduced number of photoreceptors and their synapses,
882 disruption of the outer retinal lamination, ectopic localization of GluR5, aberrant
883 rosette-like structure in the outer retina (Figures 2-4). These results suggest that
884 afadin is required for normal retinal lamination, photoreceptor cell morphology,
885 photoreceptor synapse formation, and proper GluR5 localization to OFF bipolar
886 cell dendrites. Conditional loss of AJ molecules in the retina has been reported
887 to cause partial or complete disruption of retinal lamination (Erdmann et al.,
888 2003; Fu et al., 2006; Masai et al., 2003). However, the effect of AJ molecule
889 loss on the retinal cell morphology and synapses was unclear. We revealed that
890 loss of afadin significantly but not completely reduces photoreceptor synapses.
891

892 In the *afadin* cKO mouse retina with severe outer retinal disorganization, we
893 detected the a- and b-waves of mERG and the RF of RGCs (Figures 2, 5, 7).
894 These results suggest that some visual information processing may be
895 performed by newly formed and preserved circuits even when the retinal
896 structure is severely impaired and the number of photoreceptors is remarkably
897 decreased. To our knowledge, this is the first report that the RF of RGCs could
898 be formed if several functional photoreceptors connect to BCs, even when the
899 outer retinal lamination is severely disrupted (Figure 7). The number and size of
900 RFs observed in the cKO retina were smaller than those in the cHet retina,
901 suggesting that the precise arrangement of retinal cells and lamination is

902 necessary for normal visual function. It is important to note that light stimulation
903 evoked firing responses in RGCs around the rosette-like structure, and that
904 such RGC firings could not be detected by a large distance between RGC soma
905 and MEA electrode.
906
907 We would like to speculate why the RF of RGCs was observed in the *afadin*
908 cKO retina. First, visual processing may be partially preserved without any
909 remodeling if only a small number of functional photoreceptor-BC-RGC
910 pathways remain intact. It has been shown that the RF of RGCs is detected
911 even when approximately half of cone photoreceptors are stimulated (Care et
912 al., 2019; Lee et al., 2022). Thus, in the *afadin* cKO retina, where cone
913 photoreceptors are reduced to about 40% of the cHet retina, such reduction *per*
914 *se* may not critically affect the RF organization. Furthermore, RFs of RGCs are
915 also detected in several mouse models of retinitis pigmentosa, in which rod
916 photoreceptors are degenerated and surviving cone photoreceptors lose their
917 OS discs and pedicles, instead forming abnormal processes resembling
918 synaptic dendrites (Barhoum et al., 2008; Ellis et al., 2023; Scalabrino et al.,
919 2022). A few photoreceptor-BC-RGC pathways (vertical pathways of the retina)
920 are inferred to be maintained in the cKO retina. In some regions, the density of
921 photoreceptors was high enough to make functional synapses between
922 photoreceptor and BC (Figure 2D), possibly resulting in the RF of RGCs.
923 Second, synaptic rewiring of interneurons such as BCs may recover retinal
924 function in the *afadin* cKO retina. Various studies show partial loss of
925 photoreceptors or BCs, or partial silencing of BCs causes rewiring in the

926 developing and mature retinas (Johnson and Kerschensteiner, 2014; Jones et
927 al., 1995; Okawa et al., 2014; Shen et al., 2020; Strettoi et al., 2022). Also, in
928 the *rd1* retina, neural connections between inner retinal neurons via gap
929 junctions may be enhanced, potentially resulting in the widespread distribution
930 of electrically evoked RGC responses (Ahn et al., 2022). These reports suggest
931 that reduced input from photoreceptors and BCs may lead to synaptic
932 reorganization among surviving cells. It is possible that synaptic reorganization
933 triggered by reduced photoreceptor and BC inputs may occur in the *afadin* cKO
934 retina with severe defects of the photoreceptor synapses and outer segments in
935 the developing stages, and that this might contribute to RF formation. Synaptic
936 rewiring may occur between BC dendrite and their closely located
937 photoreceptor terminal in the cKO retina. It may be necessary to count the
938 number of BC dendritic connections to each cone pedicle to verify the synaptic
939 rewiring between photoreceptor and BC, but this was quite difficult because of
940 the remarkably aberrant cone morphology in the cKO retina. As the IPL was
941 relatively intact and BC axon terminals were surrounded by many RGC
942 dendrites, synaptic reconnections between BC axon terminal and RGC dendrite
943 are presumed to be more easily established than those between photoreceptor
944 terminal and BC dendrite in the cKO retina. Thus, several BCs connected with
945 multiple functional photoreceptors may rewire to RGC dendrites and transmit
946 signals efficiently. Our findings imply that a very few BCs receiving input from
947 functional photoreceptors responded to light stimulation, and that the output
948 signal can be amplified downstream. The above two possibilities could both
949 contribute to the formation of RGC RFs. Furthermore, we cannot rule out the

950 possibility that gene expression may be changed in the *afadin* cKO retina,
951 resulting in facilitation of RF formation.
952
953 The ratio of responding to non-responding RGCs to light stimulation in the
954 *afadin* cKO retina was comparable to that in the cHet retina despite notable
955 reduction of photoreceptors (Figures 4D, 5, 6). It seems likely that the number
956 of photoreceptors connected to spreading dendrite tips of one BC may be
957 increased, and that glutamate spillover from BC terminals may contribute to
958 increasing the responsiveness of RGCs in the cKO retina because glutamate
959 transporter EAAT5 and vesicular glutamate transporter vGlut1 were similar in
960 both cKO and cHet retinas (Figures 4B, S3D, E). Glutamate released from BC
961 terminals may spread and bind GluR5, which is ectopically localized in BC
962 processes in the IPL, enhancing the response and expanding the responding
963 area (Figure 4A, B). These factors may contribute to the emergence of RF, but
964 the RF size in the cKO retina was still smaller than that in the cHet retina
965 (Figure 7). Photoreceptors in the cKO retina were reduced to 30 to 40% of the
966 cHet retina and scattered at 1M (Figures 2, 4D). The random checkerboard
967 pattern used for STA was projected onto the assumed photoreceptor layer of
968 the normal retina. However, as the morphology and position of photoreceptors
969 were disturbed in the cKO retina (Figures 2, S2D), the remaining
970 photoreceptors would be stimulated by an unfocused image with decreased
971 intensity. Accordingly, photoreceptors possibly responded weakly to unfocused
972 images, and thresholding of noise (increment >+4 SDs, decrement <-2 SDs,
973 determined by the spontaneous firing rate, see **MATERIALS and METHODS**)

may result in reduction of the RF size. Rod-driven responses were observed in RGCs in the cKO retina (Figures 5, 6). However, it is unlikely that the rod photoreceptors transmit signals to cone photoreceptors through gap junctions in the disrupted cKO outer retina, and thus, rod signals may be transmitted to RGCs via the rod BC-AII amacrine-ON cone BC pathway.

In the cKO retina, the temporal profile of RFs with short time-to-peak latency was not included (Clusters 1 and 2; Figure 7), indicating that RGCs in the cKO retina cannot respond to rapid changes in luminance. There are several ways to explain this result. For example, disruption of the outer retinal lamination may make it difficult to synchronize photoreceptor responses without gap junctions, resulting in dull responses. BCs with fast response kinetics may not be present or not functional in the cKO retina (Kuo et al., 2024). Furthermore, glutamate spillover from BC terminals may amplify the signals, but at the same time, the time-to-peak of RGC responses may be delayed. These possibilities should be investigated in the future.

Ectopic continuous AJs formed in the developing *afadin* cKO retina (Figure 9A) are possibly associated with partial disruption of retinal lamination. The *β-catenin* cKO retina also shows ectopic continuous AJs in developing stage and the disruption of the outer retinal lamination with relatively intact IPL and GCL structure in adult (Fu et al., 2006), suggesting that afadin and β-catenin are required for normal continuous AJ formation at the outer retinal surface but dispensable for maintaining AJs. The photoreceptor-specific *aPKCλ* cKO retina

998 in which AJs are dispersed in the developing stage exhibits disruption of whole
999 retinal lamination despite aPKCλ remaining in cells excluding photoreceptors.
1000 Individual cells contain AJs, but the AJs are not continuous in the *aPKCλ* cKO
1001 retina (Koike et al., 2005). These findings, based on the studies using each
1002 mutant mouse, imply that continuous AJs are important for the formation of the
1003 outer retinal structure. The ONL was severely disrupted in the cKO retina,
1004 despite the fact that afadin is not localized in the layer. The disruption is
1005 presumed to be caused by defects in AJs in the outer retina during
1006 development. In the developing *afadin* cKO retina, ectopic AJs and mislocalized
1007 progenitor cells were observed (Figure 9). These defects may lead to abnormal
1008 cell migration and positioning, ultimately resulting in ONL disorganization. In
1009 contrast, the IPL structure appeared relatively intact in the cKO retina, possibly
1010 due to functional redundancy between afadin and other cell adhesion
1011 molecules.
1012
1013 In the *afadin* cKO retina, significant increase in BCs and significant decrease in
1014 photoreceptors and Müller glial cells were observed at 1M (Figure 4D). The
1015 changes in the number and/or marker gene expression of photoreceptors and
1016 BCs were also observed in the developing cKO retina (Figure S4C-F). These
1017 results suggest that retinal cell fate was affected in the *afadin* cKO mice. As
1018 retinal cell fate is not altered in the *β-catenin* cKO retina (Fu et al., 2006), the
1019 phenotypic difference between *β-catenin* cKO and *afadin* cKO retinas may imply
1020 distinct functional properties of the in AJ molecules.
1021

One of the major concerns of retinal regeneration therapy is that while transplanted photoreceptors can form synapses with donor BCs, the transplanted tissue often shows aberrant structures, such as rosettes (Yamasaki et al., 2022). Our study demonstrated that RGCs show RFs and visual behaviors are partially preserved even when the outer retinal lamination is severely disrupted, provided that synaptic connectivity is maintained to a certain extent. Therefore, mice with photoreceptor degeneration that have undergone retinal transplantation might recognize stimulus patterns to some extent, even if aberrant structures are formed after retinal transplantation. Moreover, retinal regeneration therapy could be more effective in restoring vision than previously anticipated. In recent studies, distinct RFs of RGCs were detected in some mouse lines with progressive photoreceptor degeneration or substantial loss of cone photoreceptors or BCs, indicating the robustness of retinal circuitry (Care et al., 2019; Ellis et al., 2023; Johnson and Kerschensteiner, 2014; Lee et al., 2022; Scalabrino et al., 2022). However, whether visual function is retained in these models remains unclear. Behavioral visual responses are partially preserved in the *afadin* cKO mice, in which RFs of RGCs are reduced in number and size but clearly detectable. Given that RGCs are intact in the mouse lines used in the aforementioned studies, it is possible that visual functions are preserved to a substantial extent in those models. Although the *afadin* cKO mice responded to certain visual stimuli, the extent of what visual patterns or stimuli they can perceive remains unclear. Further detailed analyses of visual functions are required in the future.

Acknowledgments

We thank Dr. Takahisa Furukawa for providing *Dkk3*-Cre mice, Dr. Toshihiko Fujimori for providing *R26R-H2B-EGFP* mice, Takefumi Yamamoto for technical assistance in electron microscopy, Drs. Akishi Onishi, Katsunori Kitano, and Kiyo Sakagami for helpful comments, and Y. Shibata for technical assistance.

Funding

This work was supported by Grant-in-Aid for Scientific Research (B) (24390019), Fund for the Promotion of Joint International Research (22KK0137), Early-Career Scientists (23K15920), and Research Activity Start-up (22K20698) from the Japan Society for the Promotion of Science (JSPS), Takeda Science Foundation, the Kobayashi Foundation, JST PRESTO (08062795), and R-GIRO.

Author Contributions

C.K., M.T., and A.U. designed the project. Y.T. and J.M. generated *afadin flox* mice. M.H generated the ONC mice. A.U. and H.T. carried out immunohistochemical analysis. A.U. performed molecular biochemical analyses. T.K. performed electron microscopic analysis. H.O. and S.M. carried out ERG experiments. H.O. and M.W. performed multi-electrode recordings. K.S., T.N., and M.T. analyzed data of the multi-electrode recordings. A.H. carried out visual behavioral tests. A.H. and Y.E. analyzed the data of the visual behavioral tests. A.U., M.T., and C.K. wrote the manuscript. C.K. supervised the project.

1070

1071 **FIGURE LEGENDS**

1072 **Figure 1 Afadin is localized to the OS, OLM, OPL, INL, and IPL.**

1073 **A**. Immunostaining of the wild-type (WT) mouse retina (1M) with anti-afadin
1074 antibody. The afadin signals disappeared in the pre-absorbed (peptide+)
1075 sample. The signal observed in the peptide+ image represents the background
1076 and non-specific staining. Nuclei were stained with DAPI (blue).

1077 **B**. Immunostaining of the WT retinal section (1M) using anti-afadin (green)
1078 combined with anti-Nectin-1 (red) antibody. Necin-1 was partially co-localized
1079 with afadin in the OLM, OPL, and IPL.

1080 **C**. Afadin was colocalized with nectin-1, nectin-2, and nectin-3 at the OLM. The
1081 1M WT retinal sections were immunostained with anti-afadin (green), anti-
1082 nectin-1 (red, upper panels), anti-nectin-2 (red, middle panels), and anti-nectin-
1083 3 (red, lower panels) antibodies.

1084 **D**. Immunostaining of 1M WT retinal sections using anti-afadin (green), anti-
1085 SCGN (red), and anti-PKCα(white) antibodies. Afadin signals overlapped with
1086 SCGN and PKCα in the OPL and INL, and PKCα in the IPL.

1087

1088 OS, the outer segment; IS, the inner segment; OLM, the outer limiting
1089 membrane; ONL, the outer nuclear layer; OPL, the outer plexiform layer; INL,
1090 the inner nuclear layer; IPL, the inner plexiform layer; GCL, the ganglion cell
1091 layer.

1092

1093

1094 **Figure 2 Outer retinal lamination is severely disrupted in the afadin cKO**

1095 **retina.**

1096 **A**. Toluidine blue staining of the cHet and cKO mouse retinal sections at 1M.
1097 The retinal layer structure was disrupted in the cKO retina. Rod photoreceptor
1098 nuclei (insets) were deeply stained. The red asterisk indicates a rod
1099 photoreceptor. The arrowhead indicates a rosette-like structure. Scale bar in the
1100 inset, 2.5 μm.

1101 **B**. Representative images of the cHet and cKO retinas (1M) stained with anti-
1102 Rom1 (green) and anti-Rhodopsin (Rho, red) antibodies and PNA-rhodamine
1103 (white). Rom1, Rhodopsin, and PNA signals were remarkably decreased and
1104 scattered in the cKO mice. The arrowhead indicates the rosette-like structure.

1105 **C**. Representative images of the cHet and cKO retinas (1M) stained with anti-S-
1106 opsin (green) and anti-M-opsin (white) antibodies and PNA-rhodamine (red).
1107 Cone OSs were aberrantly located in the cKO retina. The arrowhead indicates
1108 the rosette-like structure.

1109 **D**. Retinal flat-mount immunostaining of the cHet and cKO retinas
1110 immunostained with anti-Arr3 (green, left panels), anti-Rom1 (green, right
1111 panels), and anti-Rhodopsin (red, right panels) antibodies. The inset, a
1112 magnified view of the area enclosed by the dashed box, shows an area with a
1113 relatively high density of photoreceptors in the cKO retina.

1114 **E**. Immunofluorescent analysis of the cHet and cKO retinas (1M) using anti-Arr3
1115 (cone marker, green in the left panels), anti-Otx2 (photoreceptor and BC
1116 marker, red in the left panels), anti-RNA binding protein with multiple splicing
1117 (RBPMS, RGC marker, green in second left panels), anti-Chx10 (BC marker,
1118 red in second left panels), anti-Lhx2 (Müller glia marker, green in third left and

third right panels), anti-AP2α (AC marker, red in third left and second right panels), and anti-Calbindin (horizontal cell and AC marker, white in third left and right panels) antibodies. Arrowheads indicate RGCs and ACs near the rosette-like structure.

F-L. Distribution of each retinal cell type based on their distance from the retinal surface in the cHet and cKO mice. The shortest distance between each cell body and either the outer or inner retinal surface was measured using ImageJ. For cones (**F**), rods (**G**), bipolar cells (**H)**, horizontal cells (**I**), and Müller glia (**J**), the distance was measured from the outer retinal surface. For amacrine cells (**K**) and retinal ganglion cells (**L**), the distance was measured from the inner retinal surface. *Note: In **K** and **L**, the X-axis is reversed such that short distance appears on the right.* The outer retinal surface was defined as the region immediately above the somata of the outer retinal cells. Bin width was 5 μm (0–5 up to 175–180 μm). Inset box plots show the distribution of raw values, with whiskers extending to 1.5 times the interquartile range and dots indicating outliers (cHet; Cone 3.45 ± 2.72 μm, n = 141 cells from 4 mice, Rod 23.1 ± 13.8 μm, n = 3055 cells from 4 mice, Bipolar cell 59.4 ± 6.74 μm, n = 432 cells from 3 mice, Horizontal cell 57.5 ± 6.45 μm, n = 20 cells from 3 mice, Müller glial cell 69.9 ± 7.61 μm, n = 191 cells from 3 mice, Amacrine cell 51.8 ± 18.6 μm, n = 362 cells from 3 mice, Ganglion cell 8.71 ± 3.71 μm, n = 93 cells from 3 mice, cKO; Cone 14.9 ± 14.2 μm, n = 42 cells from 4 mice, Rod 35.5 ± 30.5 μm, n = 716 cells from 4 mice, Bipolar cell 56.6 ± 32.7 μm, n = 1236 cells from 5 mice, Horizontal cell 37.2 ± 31.2 μm, n = 14 cells from 4 mice, Müller glial cell 45.9 ± 22.9 μm, n = 95 cells from 4 mice, Amacrine cell 63.8 ± 34.6 μm, n = 265 cells

1143 from 4 mice, Ganglion cell 38.9 ± 33.6 μm, n = 116 cells from 5 mice). ***p <
1144 0.001, **p < 0.01 by a generalized linear mixed model (GLMM) or log1p-
1145 transformation followed by a linear mixed model (LMM). Statistical tests: Cone,
1146 Rod, log1p-transformation followed by a LMM; Bipolar cell, Horizontal cell,
1147 Müller glial cell, Amacrine cell, Ganglion cell, GLMM.
1148 **M.** The thickness of the cHet and cKO retinas at 1M. (cHet; 137.9 ± 11.1 μm, n
1149 = 4, cKO; 135.5 ± 9.1 μm, n = 5). Error bars, mean ± SD. No significant
1150 difference was observed between the two groups (p = 0.735 by Student's t-test).
1151
1152
1153 **Figure 3 Photoreceptor-BC synapses were severely impaired and**
1154 **mislocalized in the afadin cKO retina.**
1155 **A**. Immunostaining of the cHet and cKO retinal sections at 1M with anti-
1156 Bassoon (green), anti-mGluR6 (red), and anti-PKCα (white) antibodies. The
1157 arrowhead indicates the synapse between rod and rod-BC. Small panels are
1158 magnified views of the area enclosed by the dashed box.
1159 **B**. Immunostaining of the cHet and cKO retinas at 1M with anti-GluR5 (green),
1160 anti-PSD95 (red), and anti-PKARIIβ (white) antibodies. The arrowhead indicates
1161 the synapse between the cone and OFF-BC. Small panels are magnified views
1162 of the area enclosed by the dashed box.
1163 **C**. 3D projection of confocal image immunostaining with anti-Bassoon (green),
1164 anti-mGluR6 (red), and anti-PKCα (white) using the cHet and cKO retina (1M).
1165 The inset, a magnified view of the area enclosed by the dashed box, shows the
1166 synapse between the rod and BC at high magnification. The arrowhead

1167 indicates the ribbon synapse between rod and rod-BC.

1168 **D**. 3D projection of confocal image immunostaining with anti-GluR5 (green),

1169 anti-PSD95 (red), and anti-PKARIIβ (white) antibodies using the cHet and cKO

1170 retina (1M).

1171 **E**. Quantification of the number of synapses between rod photoreceptor and

1172 rod-BC under 1mm^2 of retinal surface in the cHet and cKO mice immunostained

1173 with anti-Bassoon, anti-mGluR6, and anti-PKCα antibodies (cHet; 599.6 ± 49.7,

1174 n = 3, cKO; 29.1 ± 12.75, n = 4, 10 images from each mouse. Error bars, mean

1175 ± SD. ***$p < 0.001$ by a GLMM). The number of synapses decreased to about

1176 5 % of the cHet in the cKO retina.

1177 **F.** Quantification of the number of synapses between photoreceptor cells and

1178 type 3 OFF-BC under 1mm^2 of the retinal surface in the cHet and cKO mice

1179 immunostained with anti-GluR5, anti-PSD95, and anti-PKARIIβ antibodies

1180 (cHet; 24.0 ± 2.8, n = 3, cKO; 4.1 ± 1.3, n = 3, 10 images from each mouse.

1181 Error bars, mean ± SD. ***$p < 0.001$ by a GLMM). The number of synapses

1182 between the photoreceptor and Type 3 OFF-BC in the cKO retina decreased to

1183 about 15% of the cHet retina.

1184

1185

1186 **Figure 4 GluR5 is ectopically localized to ON and OFF BC processes.**

1187 **A.** Immunostaining of the cHet and cKO retinal sections at 1M with anti-GluR5

1188 (green), anti-SCGN (red), and anti-PKCα antibodies. GluR5 signal was

1189 obviously observed in the IPL of the cKO retina. Yellow and white arrowheads

1190 indicate overlap of GluR5 and PKCα, and GluR5 and SCGN, respectively. Small

1191 panels are magnified views of the area enclosed by the dashed box.

1192 **B.** Representative images of the immunostained cHet and cKO retinas (1M)

1193 with anti-GluR5 (green), anti-vGlut1 (red), and anti-SCGN (white) antibodies.

1194 **C.** Immunofluorescent analysis of the cHet and cKO retinas (1M) with anti-HPC-

1195 1 (AC marker, green in the left panels), anti-Calbindin (red in the left panels),

1196 anti-Tuj1 (RGC marker, green in the right panels), and anti-RBPMS (red in the

1197 right panels) antibodies. Arrowhead indicates acellular patches.

1198 **D.** The number of each retinal cell type per 100 μm width of retinal section at

1199 1M (cHet; Rod 185.9 ± 17.5, Cone 8.4 ± 1.4, Bipolar cell 45.5 ± 5.2, Ganglion

1200 cell 7.4 ± 1.5, Horizontal cell 2.1 ± 0.4, Amacrine cell 30.1 ± 3.2, Müller glial cell

1201 15.7 ± 2.3, n = 4, cKO; Rod 57.3 ± 17.3, Cone 3.5 ± 1.3, Bipolar cell 64.6 ± 7.8,

1202 Horizontal cell 1.9 ± 0.7, Amacrine cell 27.6 ± 6.3, Ganglion cell 5.7 ± 0.9,

1203 Müller glial cell 12.4 ± 1.5, n = 4. Error bars, mean ± SD. Horizontal cell p =

1204 0.58, AC p = 0.52, RGC p =0.10. ***p < 0.001, **p < 0.01, *p < 0.05 by Student's

1205 t test. In the cKO retina, rod and cone photoreceptors and Müller glial cells

1206 significantly decreased to about 30, 40, and 80% of the cHet retina,

1207 respectively, and BCs significantly increased to about 150% of the cHet retina.

1208 **E.** Immunofluorescent analysis of the cHet and cKO retinas at P1, P3, P5, P8,

1209 P11, and P14 using anti-Chx10 (green), anti-Otx2 (red), and anti-Ki67

1210 (progenitor cell marker, white) antibodies. NBL, the neuroblastic layer.

1211

1212

1213 **Figure 5 Reduction of the a- and b-waves in the cKO retina.**

1214 **A.** *Left*, Scotopic ERGs from the anesthetized cHet (n = 3; black) and cKO (n =

1215 3; magenta) mice. A flashlight (duration; 5 ms, white LED, intensity; 1.0×10^4
1216 cd/m^2) was applied to eyes in the dark three times. Traces: averaged (dark) and
1217 SD (pale). *Right*, Photopic ERGs. The anesthetized cHet (black) and cKO
1218 (magenta) mice were light (31.6 cd/m^2) adapted for 10 min, and then, a
1219 flashlight (duration; 5 ms, intensity; 1.0×10^4 cd/m^2) was superimposed on the
1220 adapted light to eyes 16 times.
1221 **B.** mERGs recorded by MEA from the cHet (black) and cKO (magenta) retinas.
1222 A flashlight (duration; 5 ms, green LED; λ_{max} = 510 nm, intensity; 2.5×10^4
1223 photon/s/μm^2) was applied to the isolated whole retina 3 times every 10 s.
1224 Control (solid line), L-AP4 (10 μM) (pale), and after washout (dotted line). *Left*,
1225 cHet; SD of the amplitude for 200 ms after the flash onset; >1,000 μV, 292/413
1226 electrodes, n = 7 retinas from 4 mice. *Right*, cKO; SD of the amplitude for 300
1227 ms after the flash onset; >50 μV, 13/590 electrodes, n = 10 retinas from 6 mice.
1228 **C.** *Left*, Amplitude of the a-wave (cHet; 155 ± 58.7 μV, n = 292 electrodes, n = 7
1229 retinas from 4 mice, cKO; 44.1 ± 21.7 μV, n = 13 electrodes, n = 10 retinas from
1230 6 mice, Error bars, mean ± SD. ***$p < 0.001$, Mann-Whitney U test). *Right*,
1231 Amplitude of the b-wave (cHet; 163 ± 76.5 μV, n = 292 electrodes, cKO; 28.4 ±
1232 19.6 μV, n = 13 electrodes, $p = 7.08 \times 10^{-9}$, Mann-Whitney U test).
1233 **D.** Ratio of b-wave amplitude / a-wave amplitude (b / a) (cHet; 1.19 ± 0.67, cKO;
1234 0.59 ± 0.23, Error bars, mean ± SD. ***$p < 0.001$, Mann-Whitney U test).
1235 **E.** *Left*, Implicit time of the a-wave (cHet; 62.6 ± 10.8 ms, n = 292 electrodes,
1236 cKO; 149 ± 16.0 ms, n = 13 electrodes, $p = 5.34 \times 10^{-10}$, Mann-Whitney U test).
1237 *Right*, Implicit time of the b-wave (cHet; 127 ± 25.3 ms, n = 292 electrodes,
1238 cKO; 229 ± 60.7 ms, n = 13 electrodes, Error bars, mean ± SD. ***$p < 0.001$,

1239 Mann-Whitney U test).

1240 **F.** Difference between implicit time of the b-wave and that of the a-wave (cHet;

1241 64.4 ± 22.0 ms, n = 292 electrodes, cKO; 80.4 ± 50.9 ms, n = 13 electrodes,

1242 Error bars, mean ± SD. p = 0.40, Mann-Whitney U test).

1243

1244

1245 **Figure 6 RGC classification based on the light-evoked responses.**

1246 **A, B.** Representative light-evoked responses. **A**, The cHet retina. **B**, The cKO

1247 retina. A flash (duration; 2 s, intensity; 24.2 or 27.3 cd/m^2) was applied seven

1248 times every 8 s. After spike sorting, the raster plots (*top*) and the PSTHs

1249 (*bottom*) were created (20 ms/bin). Based on the PSTHs, RGC responses were

1250 classified into “ON”, “ON-OFF”, “ON-OFF inhibition”, “OFF”, and “None” types.

1251 **C**. Ratio of responded to non-responded types (cHet; n = 434, cKO; n = 388).

1252 **D**. Rod and cone inputs to RGCs (cHet; n = 434, cKO; n = 388). 2-s green LED

1253 flash (λ_{max} = 510 nm, intensity; 4.8 x 10^3 photons/s/μm^2) and UV LED flash (λ_{max}

1254 = 360 nm, intensity; 3.3 x 10^4 photons/s/μm^2) were applied 7 times every 8 s to

1255 stimulate mainly rods and S cones, respectively.

1256

1257

1258 **Figure 7 Spatiotemporal properties of the RF of RGCs.**

1259 **A**. *Left*, An isolated retina on the MEA. Electrodes (black square), mapped RFs

1260 (colored oval), and the region where immunohistochemical examination was

1261 performed after recording (magenta square). Scale bar 200 μm. *Right*,

1262 Immunohistochemical staining with anti-PKARIIβ (green), anti-PSD95 (red), and

1263 anti-PKCα (white) antibodies. IPL: the inner plexiform layer.

1264 **B**. Number of cells whose RF was clearly observed (cHet; 195/434 cells, n = 4

1265 retinas, cKO; 69/388 cells, n = 4 retinas).

1266 **C**. The spatial profile of RFs in the cHet (*Top*) and cKO (*Bottom*) retinas. Color

1267 scale illustrates high (red) to low (blue) relative to the average (green). Scale

1268 bar 100 μm.

1269 **D**. RF size of the cKO retina was significantly smaller than that of the cHet

1270 retina (cHet; 0.0307 ± 0.0210 mm^2 n = 195, n = 4 retinas, cKO; 0.0161 ±

1271 0.00839 mm^2 n = 69, n = 4 retinas, Error bars, mean ± SD. ***$p < 0.001$, Mann-

1272 Whitney U test).

1273 **E**. Short and long axes of the oval fitted to each RF.

1274 **F**. Clustering of RGCs based on the temporal profile of RFs. Five clusters were

1275 visualized (cHet; circle, n = 4 retinas, cKO; x, n = 4 retinas).

1276 **G**. Temporal profiles from each cluster were superimposed separately (cHet;

1277 black, cKO; magenta, mean; solid line, SD: pale line).

1278 **H**. Time-to-peak latency of the temporal profile (cHet; filled bar, cKO; open bar).

1279 Mean ± SD. (cHet; cluster 1; -113 ± 15 msec, n = 31, cluster 2; -111 ± 13 msec,

1280 n = 36, cluster 3; -200 ± 31 msec, n = 51, cluster 4; -171 ± 19 msec, n = 37,

1281 cluster 5; -178 ± 28 msec, n = 40, cKO; cluster 3; -163 ± 21 msec, n = 10,

1282 cluster 4; -238 ± 34 msec, n = 36, cluster 5; -217 ± 41 msec, n = 23).

1283

1284

1285 **Figure. 8 Visual function is partially retained in the *afadin* cKO mice.**

1286 **A.** Schematic diagram of the experimental setup for the OMR test. Drifting

square-wave gratings were displayed on monitors surrounding the mouse, and head-tracking movements were recorded under photopic conditions.

B. Representative traces of head-tracking movements in the cHet, cKO, and ONC mice. Blue lines indicate head movement trajectories, and red segments denote the periods when the head movement aligned with the direction and timing of the visual stimulus.

C. Summary of head-tracking movements in response to drifting gratings with spatial frequencies of 0.056, 0.10, and 0.27 cycles/degree, as well as under no-stimulus conditions, in the cHet, cKO, and ONC mice (cHet; 0.056 cycles/degree 7.30 ± 1.94, 0.10 cycles/degree 7.89 ± 2.00, 0.27 cycles/degree 7.16 ± 1.39, n = 8 mice, cKO; 0.056 cycles/degree 2.36 ± 1.59, 0.10 cycles/degree 1.64 ± 1.29, 0.27 cycles/degree 0.0268 ± 0.103, n = 14 mice, ONC; 0.056 cycles/degree 0.0833 ± 0.121, 0.10 cycles/degree 0.0714 ± 0.161, 0.27 cycles/degree 0.0476 ± 0.128, n = 7 mice). Error bars, mean ± SD. No stimulus; cHet vs cKO $p > 0.9999$, cHet vs ONC $p > 0.9999$, cKO vs ONC $p > 0.9999$, 0.27 cycles/degree; cKO vs ONC $p > 0.9999$. ***$p < 0.001$, Dunn's test.

D. Comparison of head-tracking responses across spatial frequencies (0.056, 0.10, and 0.27 cycles/degree). Statistical comparisons were conducted within each mouse group. No significant differences were detected across spatial frequencies in cHet and ONC mice. In contrast, the cKO mice exhibited a trend toward decreased head-tracking responses with increasing spatial frequency. Error bars, mean ± SD. cHet; 0.056 cycles/degree vs 0.1 cycles/degree $p = 0.3566$, 0.1 cycles/degree vs 0.27 cycles/degree $p = 0.2606$, 0.056 cycles/degree vs 0.27 cycles/degree $p > 0.9999$, cKO; 0.056 cycles/degree vs

1311 0.1 cycles/degree $p = 0.2577$. ***$p < 0.001$, Dunn's test.

1312 **E.** Schematic diagram of the visual cliff test. The apparatus consists of a single

1313 transparent platform spanning two arenas with identical checkerboard patterns:

1314 one immediately beneath the platform (the shallow side) and the other on the

1315 floor (the deep side), creating a visual cliff. Mice are placed at the boundary

1316 between the two sides, and their location preference is evaluated.

1317 **F.** Time spent on the shallow side during the visual cliff test. The percentage of

1318 time spent on the shallow side was significantly higher in the cHet mice than in

1319 the cKO and ONC mice. No significant difference was observed between the

1320 cKO and ONC mice (cHet; 81.1 ± 14.6, n = 19 mice, cKO; 57.4 ± 17.6, n = 26

1321 mice, ONC; 51.1 ± 6.38, n = 6 mice). Error bars, mean ± SD. ***$p < 0.001$, one-

1322 way ANOVA followed by Tukey's multiple comparisons test.

1323

1324

1325 **Figure. 9 Ectopic AJs are observed in the developing *afadin* cKO retina.**

1326 **A.** Immunostaining of the cHet and cKO retinas at postnatal day 0 (P0) with

1327 anti-phospho-histone H3S10 (pHH3, mitotic cell marker, green), anti-N-

1328 Cadherin (red in left, second left, and second right panels), anti-Nectin-1 (white

1329 in left, second left, and third right panels), anti-β-catenin (red in the right panels)

1330 antibodies. Ectopic N-cadherin, nectin-1, and β-catenin signals were observed

1331 in the cKO retinas, and pHH3-positive cells were localized near these ectopic

1332 signals.

1333 **B.** Quantification of pHH3-positive cells per 100 μm width of retinal sections in

1334 the cHet and cKO retinas at P0 (cHet; 4.40 ± 0.937, n = 3, cKO; 6.69 ± 0.507, n

1335 = 4). pHH3 positive cells significantly increased in the cKO retina. Error bars,
1336 mean ± SD. **$p < 0.01$ by Student's t-test).
1337 **C.** Retinal sections from the cHet and cKO mice immunostained with anti-pHH3
1338 antibody (red) at P1 (upper panels), P3 (middle panels), and P5 (lower panels).
1339 **D.** Distribution of mitotic cells based on their distance from the outer retinal
1340 surface in the cHet and cKO mice at P1 (top), P3 (middle), and P5 (bottom).
1341 The shortest distance between mitotic cell body and the outer retinal surface
1342 was measured using ImageJ. Bin width was 5 μm (0–5 up to 245–250 μm).
1343 Inset box plots show the distribution of raw values, with whiskers extending to
1344 1.5 times the interquartile range and dots indicating outliers (cHet; P1 3.76 ±
1345 17.5 μm, n = 300 cells from 5 mice, P3 6.73 ± 28.8 μm, n = 469 cells from 3
1346 mice, P5 16.7 ± 44.7 μm, n = 180 cells from 4 mice, cKO; P1 48.4 ± 24.1 μm, n
1347 = 326 cells from 4 mice, P3 76.0 ± 41.9 μm, n = 902 cells from 4 mice, P5 94.0
1348 ± 44.8 μm, n = 163 cells from 4 mice). ***$p < 0.001$ by log1p-transformation
1349 followed by a LMM.
1350 **E.** Retinal sections from the cHet and cKO mice immunostained with anti-BrdU
1351 antibody (green) at P1 (upper panels), P3 (middle panels), and P5 (lower
1352 panels).
1353 **F.** Distribution of progenitor cells based on their distance from the outer retinal
1354 surface in the cHet and cKO mice at P1 (top), P3 (middle), and P5 (bottom). Bin
1355 width was 5 μm (0–5 up to 245–250 μm). Inset box plots show the distribution of
1356 raw values, with whiskers extending to 1.5 times the interquartile range and
1357 dots indicating outliers (cHet; P1 58.0 ± 22.1 μm, n = 2527 cells from 4 mice, P3
1358 83.5 ± 31.7 μm, n = 1904 cells from 4 mice, P5 95.3 ± 32.4 μm, n = 620 cells

1359 from 5 mice, cKO; P1 62.7 ± 35.2 μm, n = 1713 cells from 4 mice, P3 96.5 ±
1360 48.5 μm, n = 2025 cells from 3 mice, P5 90.7 ± 40.5 μm, n = 630 cells from 3
1361 mice). P5 $p = 0.49$, ***$p < 0.001$, **$p < 0.01$ by log1p-transformation followed by
1362 a LMM.
1363
1364
1365 **Figure S1 Afadin is localized to AJs in developing and mature retinas.**
1366 **A**. Immunostaining of the WT retinal section (1 M) with anti-afadin (green)
1367 antibody combined with nectin-2 (red, upper and middle panels) and nectin-3
1368 (red, lower panels) antibodies. Nectin-2 and nectin-3 were localized in the OLM.
1369 The nectin-2 signal in the IPL was insufficient for reliable assessment of its
1370 localization and colocalization.
1371 **B**. Immunostaining with anti-afadin (green), anti-nectin-1 (red), and anti-Arr3 (a
1372 cone marker, white) antibodies. Afadin was co-localized with nectin-1 in cone
1373 synapses.
1374 **C**. Immunostaining of the WT retinal section (P0) with anti-afadin (green) and
1375 anti-nectin-1 (red) antibodies.
1376
1377
1378 **Figure S2 AJs in the OLM are disrupted in the afadin cKO retina.**
1379 **A, B.** Immunostaining of *Dkk3*-Cre; *R26R-H2B-EGFP* and *R26R-H2B-EGFP*
1380 retinas at P0 (**A**) and 1M (**B**) using an anti-GFP antibody (green). The Cre
1381 recombinase activity was detected in the *Dkk3*-Cre; *R26R-H2B-EGFP* retina at
1382 both stages.

1383 **C**. Western blot analysis of the cHet and cKO retinas using anti-afadin (upper
1384 panel) and anti-GAPDH (lower panel) antibodies. No significant afadin band
1385 was detected in the cKO retina.
1386 **D.** Electron microscopic analysis of the cHet and cKO retinas (1M). A few
1387 ectopic disc structures were observed in the cKO retina. The inset, a magnified
1388 view of the area enclosed by the dashed box, shows the ectopic disc structure
1389 at high magnification. The arrowhead indicates the outer segment disc
1390 structure. RPE, the retinal pigment epithelium.
1391 **E.** Immunostaining of the cHet and cKO retinal sections at 1M using anti-β-
1392 catenin (green, left panels), anti-nectin-1 (red, left panels), and anti-N-cadherin
1393 (green, right panels). Signals of these markers were not observed at the outer
1394 retinal surface in the cKO mice.
1395 **F.** Immunostaining of the cHet and cKO retinal sections at 1M using anti-
1396 glutamine synthetase (GS, green) antibody. Obvious GS signals were observed
1397 in the inner side of the retina but not at the outer retinal surface in the cKO
1398 mice.
1399 **G.** Retinal sections from the cHet and cKO mice at 1M were stained with an
1400 anti-CD31 antibody (red). No notable vascular differences were observed in the
1401 cKO retina.
1402
1403
1404 **Figure S3 The OS and photoreceptor-BC synapses are affected in the**
1405 **developing afadin cKO retina.**
1406 **A**. Immunostaining of the cHet and cKO retinas at 1M with anti-PKCα (green),

1407 anti-PSD95 (red) antibodies. Small panels are magnified views of the area
1408 enclosed by the dashed box.
1409 **B**. 3D projection of confocal image immunostaining with anti-PKCα (green),
1410 anti-PSD95 (red) antibodies.
1411 **C**. Quantification of the number of contacts between photoreceptor and rod ON-
1412 BC under 1mm^2 of retinal surface in the cHet and cKO mice immunostained
1413 with anti-GluR5, anti-PSD95, and anti-PKARIIβ antibodies (cHet; 550.5 ± 29.1,
1414 n = 3, cKO; 65.2 ± 7.9, n = 3, 10 images from each mouse. Error bars, mean ±
1415 SD ***p < 0.001 by a LMM). The number of synapses between the rod and ON
1416 BC decreased to about 10% of the cHet in the cKO retina.
1417 **D, E.** The cHet and cKO retinas (1M) stained with anti-EAAT5 (green), anti-
1418 SCGN (red in **D**), and anti-PKCα (white in **D**), anti-PSD95 (red in **E**) antibodies
1419 and PNA-rhodamine (white in **E**). Glutamate transporter EAAT5 localization to
1420 ON and OFF BC axon terminals and photoreceptor axon terminals were
1421 unaffected in the cKO retina. Small panels are magnified views of the area
1422 enclosed by the dashed box.
1423 **F.** Immunostaining of the cHet and cKO retinal sections at 1M with anti-ChAT
1424 (green), anti-Calretinin (red), and anti-Calbindin (white) antibodies. Obvious
1425 ChAT bands, Calretinin bands, and Calbindin bands were observed in the IPL of
1426 the cKO mice.
1427
1428
1429 **Figure S4 Retinal cell fate determination is altered during development in**
1430 **the *afadin* cKO mice.**

1431 **A.** The number of PKCα+ and SCGN+ cells per 100 μm width of retinal sections
1432 at 1M (cHet; PKCα+ 15.8 ± 2.6, SCGN+ 24.7 ± 4.8, n = 4, cKO; PKCα+ 23.6 ±
1433 5.2, SCGN+ 37.4 ± 7.7, n = 4. Error bars, mean ± SD. *$p < 0.05$ by Student's t-
1434 test). PKCα+ cells and SCGN+ cells significantly increased to 150% of the cHet.
1435 **B.** The number of PKCα+ cell processes in the IPL per 100 μm width of retinal
1436 sections at 1M (cHet; 18.6 ± 0.5, n = 4, cKO; 14.7 ± 1.2, n = 4. Error bars, mean
1437 ± SD. ***$p < 0.01$ by Student's t-test). The number of PKCα+ cell processes
1438 significantly decreased to 80% of the cHet.
1439 **C.** The number of each retinal cell types per 100 μm width of retinal sections at
1440 P14 (cHet; Rod 176.5± 14.3, Cone 10.6 ± 1.3, Bipolar cell 49.2 ± 1.9, Ganglion
1441 cell 8.1 ± 0.8, Horizontal cell 2.5 ± 0.7, Amacrine cell 30.3 ± 2.1, Müller glial cell
1442 17.3 ± 1.4, n = 4, cKO; Rod 98.3 ± 3.8, Cone 4.7 ± 0.9, Bipolar cell 76.8 ± 10.3,
1443 Horizontal cell 1.9 ± 0.8, Amacrine cell 32.2 ± 8.9, Ganglion cell 8.5 ± 1.0,
1444 Müller glial cell 17.2 ± 3.3, n = 3. Error bars, mean ± SD. Horizontal cell p =
1445 0.36, Amacrine cell p = 0.68, Ganglion cell p =0.57, Müller glial cell p = 0.94.
1446 ***$p < 0.001$ by Student's t-test). Rod and cone photoreceptors were
1447 significantly reduced to approximately 55% and 45%, respectively, of those in
1448 the cHet retina, while BCs significantly increased to approximately 150% in the
1449 cKO retina.
1450 **D.** Expression of photoreceptor and BC marker genes in the cHet and cKO at
1451 P14 (Opn1sw and Opn1mw; cone maker, Nrl and Rhodopsin; rod marker,
1452 Chx10; BC marker, Trpm1 and mGluR6; ON BC marker). Each gene expression
1453 level was normalized to GAPDH, a housekeeping gene. The expression of Nrl,
1454 Rhodopsin, Opn1sw, and Opn1mw significantly decreased, whereas the

1455 expression of mGluR6, Trpm1, and Chx10 significantly increased in the cKO
1456 retina. Error bars, mean ± SD. ***$p < 0.001$, **$p < 0.01$. Statistical tests: Opn1sw
1457 Welch's t-test; Opn1mw Student's t-test; Nrl Welch's t-test; Rho Student's t-test;
1458 Chx10 Welch's t-test; Trpm1 Student's t-test; mGluR6 Student's t-test.
1459 **E.** The number of BCs per 100 μm width of retinal sections at P1, P3, and P5
1460 (cHet; P1 4.42 ± 1.09, n = 5, P3 17.2 ± 2.47, n = 3, P5 59.9 ± 7.42, n = 4, cKO;
1461 P1 4.71 ± 1.75, n = 4, P3 18.7 ± 1.74, n = 4, P5 96.4 ± 6.91, n = 3). BCs
1462 (Chx10-positive and Ki67-negative) were significantly increased in the cKO
1463 retina at P5, but not at P1 or P3. Error bars, mean ± SD. P1 $p = 0.77$, P3 $p =$
1464 0.56, **$p < 0.01$ by Student's t-test.
1465 **F.** Expression of rod photoreceptor cell marker genes (Rho and Nrl) in the cHet
1466 and cKO at P1, P3, and P5. Each gene expression was normalized to GAPDH,
1467 a housekeeping gene. The expression of Nrl and Rhodopsin significantly
1468 decreased in the cKO retina at P5. No significant difference was observed at P1
1469 and P3. Error bars, mean ± SD. P1: Nrl $p = 0.50$, Rho $p = 0.81$, P3: Nrl $p = 0.97$,
1470 Rho $p = 0.81$, *$p < 0.05$. Statistical tests: P1 Rho, Mann–Whitney U test; P1 Nrl,
1471 P3 Rho, P3 Nrl, P5 Nrl, and P5 Rho, Student's t-test.
1472
1473
1474 **Figure S5 Retinal lamination is disputed in the *afadin* cKO retina during**
1475 **development.**
1476 **A**. Immunostaining of the cHet and cKO retinal sections at P1, P3, P5, P8, P11,
1477 and P14 with anti-HPC-1 (green), anti-RBPMS (red) antibodies. Yellow and
1478 white arrowheads indicate acellular patches and aberrant acellular regions not

1479 containing IPL components, respectively.

1480 **B**. Immunostaining of the cHet and cKO retinal sections at P1, P3, P5, P8, P11,
1481 and P14 with anti-AP2α (green), anti-Calbindin (red) antibodies. Yellow and
1482 white arrowheads indicate acellular patches and aberrant acellular regions not
1483 containing IPL components, respectively.

1484 **C**. Immunostaining of the cHet and cKO retinal sections at P8, P11, and P14
1485 with anti-Rom1 (green), anti-Rho (red) antibodies. Yellow and white arrowheads
1486 indicate the rosette-like structure and aberrant acellular regions not containing
1487 Rom1 and Rho signals, respectively.

1488 **D.** Representative images of the cHet and cKO retinas (P11) stained with
1489 antibodies against PKARIIβ (green, left panels), Arr3 (red, left panels), Bassoon
1490 (green, right panels), mGluR6 (red, right panels), PKCα (white, right panels).
1491 The inset, a magnified view of the area enclosed by the dashed box, shows the
1492 synapse between Cone and Type 3 OFF-BC (left panels), and ribbon synapses
1493 (right panels) at high magnification.

1494

1495

1496 **Figure. S6 The number of apoptotic cells decreased in the developing cKO**
1497 **retina.**

1498 **A.** Immunostaining of the cHet and cKO retinas (1M) with anti-active caspase 3
1499 (AC3, green) antibody. Arrowhead indicates AC3 positive cell.

1500 **B.** Quantification of apoptotic cells per 1mm^2 in the cHet and cKO retinas at P1,
1501 P3, P5, P14, and 1M (cHet; P1 176.9 ± 31.0, n = 4, P3 164.7 ± 33.4, n = 3, P5
1502 112.1 ± 25.8, n = 4, P14 13.7 ± 4.5, n = 5, 1M 0.577 ± 0.699, n = 4, cKO; P1

322.1 ± 65.5, n = 4, P3 cKO; 267.4 ± 29.1, n = 3, P5 177.1 ± 36.0, n = 4, P14 86.4 ± 17.3, n = 3, 1M 66.7 ± 8.2, n = 5). Apoptotic cells significantly increased in the cKO retina. Error bars, mean ± SD. *$p < 0.05$, **$p < 0.01$. Statistical tests: P1, P3, P5 Student's t-test; P14 Mann–Whitney U test; 1M Welch's t-test.

C. Quantification of progenitor cells labeled by BrdU per 100 μm width of retinal section in the cHet and cKO retinas at P1, P3, and P5 (cHet; P1 70.8 ± 7.64, n = 4, P3 66.6 ± 17.0, n = 4, P5 17.6 ± 8.87, n = 3. cKO; P1 63.2 ± 7.31, n = 4, P3 65.1 ± 2.15, n = 3, P5 31.8 ± 5.03, n = 3). There was no significant difference between the cHet and cKO retinas. Error bars, mean ± SD. P1 $p = 0.20$, P3 $p = 0.87$, P5 $p = 0.074$. Statistical tests: P1, P5 Student's t-test; P3 Welch's t-test.

D. Quantification of the retinal thickness in the cHet and cKO mice at P1, P3, and P5 (cHet; P1 145.1 ± 16.6, n = 5, P3 190.2 ± 9.81, n = 4, P5 203.9 ± 26.6, n = 5. cKO; P1 139.2 ± 26.1, n = 4, P3 203.7 ± 21.6, n = 5, P5 200.0 ± 26.7, n = 4). There was no significant difference between the cHet and cKO retinas. Error bars, mean ± SD. P1 $p = 0.54$, P3 $p = 0.29$, P5 $p = 1.0$. Statistical tests: P1, P3 Student's t-test; P5 Mann–Whitney U test.

REFERENCES

Abe T, Kiyonari H, Shioi G, Inoue K-I, Nakao K, Aizawa S, Fujimori T. 2011. Establishment of conditional reporter mouse lines at ROSA26 locus for live cell imaging. *Genesis* **49**:579–590.

Ahn J, Cha S, Choi K-E, Kim S-W, Yoo Y, Goo YS. 2022. Correlated activity in the degenerate retina inhibits focal response to electrical stimulation. *Front Cell Neurosci* **16**:889663.

Amini R, Rocha-Martins M, Norden C. 2017. Neuronal migration and lamination in the vertebrate retina. *Front Neurosci* **11**:742.

Ayala R, Shu T, Tsai L-H. 2007. Trekking across the brain: the journey of neuronal migration. *Cell* **128**:29–43.

Barhoum R, Martínez-Navarrete G, Corrochano S, Germain F, Fernandez-Sanchez L, de la Rosa EJ, de la Villa P, Cuenca N. 2008. Functional and structural modifications during retinal degeneration in the rd10 mouse. *Neuroscience* **155**:698–713.

Baum B, Georgiou M. 2011. Dynamics of adherens junctions in epithelial establishment, maintenance, and remodeling. *J Cell Biol* **192**:907–917.

Cameron EG, Xia X, Galvao J, Ashouri M, Kapiloff MS, Goldberg JL. 2020. Optic nerve crush in mice to study retinal ganglion cell survival and regeneration. *Bio Protoc* **10**. doi:10.21769/BioProtoc.3559

Cao Y, Sarria I, Fehlhaber KE, Kamasawa N, Orlandi C, James KN, Hazen JL, Gardner MR, Farzan M, Lee A, Baker S, Baldwin K, Sampath AP, Martemyanov KA. 2015. Mechanism for selective synaptic wiring of rod photoreceptors into the retinal circuitry and its role in vision. *Neuron* **87**:1248–1260.

Care RA, Kastner DB, De la Huerta I, Pan S, Khoche A, Della Santina L, Gamlin C, Santo Tomas C, Ngo J, Chen A, Kuo Y-M, Ou Y, Dunn FA. 2019. Partial cone loss triggers synapse-specific remodeling and spatial receptive field rearrangements in a mature retinal circuit. *Cell Rep* **27**:2171-2183.e5.

Choi H, Zhang L, Cembrowski MS, Sabottke CF, Markowitz AL, Butts DA, Kath WL, Singer JH, Riecke H. 2014. Intrinsic bursting of AII amacrine cells underlies oscillations in the rd1 mouse retina. *J Neurophysiol* **112**:1491–1504.

Clarke G, Goldberg AF, Vidgen D, Collins L, Ploder L, Schwarz L, Molday LL, Rossant J, Szél A, Molday RS, Birch DG, McInnes RR. 2000. Rom-1 is required for rod photoreceptor viability and the regulation of disk morphogenesis. *Nat Genet* **25**:67–73.

de Ligt J, Willemsen MH, van Bon BWM, Kleefstra T, Yntema HG, Kroes T, Vulto-van Silfhout AT, Koolen DA, de Vries P, Gilissen C, del Rosario M, Hoischen A, Scheffer H, de Vries BBA, Brunner HG, Veltman JA, Vissers LELM. 2012. Diagnostic exome sequencing in persons with severe intellectual disability. *N Engl J Med* **367**:1921–1929.

Dräger UC. 1981. Observations on the organization of the visual cortex in the reeler mouse. *J Comp Neurol* **201**:555–570.

Duan X, Krishnaswamy A, De la Huerta I, Sanes JR. 2014. Type II cadherins

1566 guide assembly of a direction-selective retinal circuit. *Cell* **158**:793–807.
1567 Duan X, Krishnaswamy A, Laboulaye MA, Liu J, Peng Y-R, Yamagata M, Toma
1568 K, Sanes JR. 2018. Cadherin combinations recruit dendrites of distinct
1569 retinal neurons to a shared interneuronal scaffold. *Neuron* **99**:1145-
1570 1154.e6.
1571 Ellis EM, Paniagua AE, Scalabrino ML, Thapa M, Rathinavelu J, Jiao Y,
1572 Williams DS, Field GD, Fain GL, Sampath AP. 2023. Cones and cone
1573 pathways remain functional in advanced retinal degeneration. *Curr Biol*
1574 **33**:1513-1522.e4.
1575 Erdmann B, Kirsch F-P, Rathjen FG, Moré MI. 2003. N-cadherin is essential for
1576 retinal lamination in the zebrafish. *Dev Dyn* **226**:570–577.
1577 Fox MW. 1965. The visual cliff test for the study of visual depth perception in the
1578 mouse. *Anim Behav* **13**:232–233.
1579 Fu X, Sun H, Klein WH, Mu X. 2006. Beta-catenin is essential for lamination but
1580 not neurogenesis in mouse retinal development. *Dev Biol* **299**:424–437.
1581 Gil-Sanz C, Landeira B, Ramos C, Costa MR, Müller U. 2014. Proliferative
1582 defects and formation of a double cortex in mice lacking Mltt4 and Cdh2
1583 in the dorsal telencephalon. *J Neurosci* **34**:10475–10487.
1584 Gollisch T, Meister M. 2010. Eye smarter than scientists believed: neural
1585 computations in circuits of the retina. *Neuron* **65**:150–164.
1586 Greenwald SH, Kuchenbecker JA, Roberson DK, Neitz M, Neitz J. 2014. S-
1587 opsin knockout mice with the endogenous M-opsin gene replaced by an
1588 L-opsin variant. *Vis Neurosci* **31**:25–37.
1589 Guy J, Staiger JF. 2017. The functioning of a cortex without layers. *Front*
1590 *Neuroanat* **11**:54.
1591 Guy J, Wagener RJ, Möck M, Staiger JF. 2015. Persistence of functional
1592 sensory maps in the absence of cortical layers in the somsatosensory
1593 cortex of reeler mice. *Cereb Cortex* **25**:2517–2528.
1594 Harris TJC, Tepass U. 2010. Adherens junctions: from molecules to
1595 morphogenesis. *Nat Rev Mol Cell Biol* **11**:502–514.
1596 Haverkamp S, Ghosh KK, Hirano AA, Wässle H. 2003. Immunocytochemical
1597 description of five bipolar cell types of the mouse retina. *J Comp Neurol*
1598 **455**:463–476.
1599 Hori T, Fukutome M, Maejima C, Matsushima H, Kobayashi Kensuke, Kitazawa
1600 S, Kitahara R, Kitano K, Kobayashi Kenta, Moritoh S, Koike C. 2019.
1601 Gene delivery to cone photoreceptors by subretinal injection of rAAV2/6
1602 in the mouse retina. *Biochem Biophys Res Commun* **515**:222–227.
1603 Ikeda W, Nakanishi H, Miyoshi J, Mandai K, Ishizaki H, Tanaka M, Togawa A,
1604 Takahashi K, Nishioka H, Yoshida H, Mizoguchi A, Nishikawa S, Takai Y.
1605 1999. Afadin: A key molecule essential for structural organization of cell-
1606 cell junctions of polarized epithelia during embryogenesis. *J Cell Biol*
1607 **146**:1117–1132.
1608 Inagaki M, Irie K, Ishizaki H, Tanaka-Okamoto M, Morimoto K, Inoue E, Ohtsuka
1609 T, Miyoshi J, Takai Y. 2005. Roles of cell-adhesion molecules nectin 1
1610 and nectin 3 in ciliary body development. *Development* **132**:1525–1537.
1611 Johnson RE, Kerschensteiner D. 2014. Retrograde plasticity and differential
1612 competition of bipolar cell dendrites and axons in the developing retina.

Curr Biol **24**:2301–2306.
Jones BW, Marc RE, Pfeiffer RL. 1995. Retinal degeneration, remodeling and plasticityWebvision: The Organization of the Retina and Visual System. Salt Lake City (UT): University of Utah Health Sciences Center.
Koike C, Nishida A, Akimoto K, Nakaya M-A, Noda T, Ohno S, Furukawa T. 2005. Function of atypical protein kinase C lambda in differentiating photoreceptors is required for proper lamination of mouse retina. *J Neurosci* **25**:10290–10298.
Kretschmer F, Kretschmer V, Kunze VP, Kretzberg J. 2013. OMR-arena: automated measurement and stimulation system to determine mouse visual thresholds based on optomotor responses. *PLoS One* **8**:e78058.
Kretschmer F, Sajgo S, Kretschmer V, Badea TC. 2015. A system to measure the Optokinetic and Optomotor response in mice. *J Neurosci Methods* **256**:91–105.
Kubo S, Yamamoto H, Kajimura N, Omori Y, Maeda Y, Chaya T, Furukawa T. 2021. Functional analysis of Samd11, a retinal photoreceptor PRC1 component, in establishing rod photoreceptor identity. *Sci Rep* **11**:4180.
Kuo SP, Yu W-Q, Srivastava P, Okawa H, Santina LD, Berson DM, Awatramani GB, Wong ROL, Rieke F. 2024. Cone bipolar cell synapses generate transient versus sustained signals in parallel ON pathways of the mouse retina. *bioRxiv*. doi:10.1101/2024.05.13.593825
Lee JY, Care RA, Kastner DB, Della Santina L, Dunn FA. 2022. Inhibition, but not excitation, recovers from partial cone loss with greater spatiotemporal integration, synapse density, and frequency. *Cell Rep* **38**:110317.
Liu JS. 2011. Molecular genetics of neuronal migration disorders. *Curr Neurol Neurosci Rep* **11**:171–178.
Majima T, Ogita H, Yamada T, Amano H, Togashi H, Sakisaka T, Tanaka-Okamoto M, Ishizaki H, Miyoshi J, Takai Y. 2009. Involvement of afadin in the formation and remodeling of synapses in the hippocampus. *Biochem Biophys Res Commun* **385**:539–544.
Mangeol P, Massey-Harroche D, Sebbagh M, Richard F, Le Bivic A, Lenne P-F. 2024. The zonula adherens matura redefines the apical junction of intestinal epithelia. *Proc Natl Acad Sci U S A* **121**:e2316722121.
Masai I, Lele Z, Yamaguchi M, Komori A, Nakata A, Nishiwaki Y, Wada H, Tanaka H, Nojima Y, Hammerschmidt M, Wilson SW, Okamoto H. 2003. N-cadherin mediates retinal lamination, maintenance of forebrain compartments and patterning of retinal neurites. *Development* **130**:2479–2494.
Masland RH. 2012. The neuronal organization of the retina. *Neuron* **76**:266–280.
Meng W, Takeichi M. 2009. Adherens junction: molecular architecture and regulation. *Cold Spring Harb Perspect Biol* **1**:a002899.
Miao GG, Smeyne RJ, D'Arcangelo G, Copeland NG, Jenkins NA, Morgan JI, Curran T. 1994. Isolation of an allele of reeler by insertional mutagenesis. *Proc Natl Acad Sci U S A* **91**:11050–11054.
Mitchiner JC, Pinto LH, Vanable JW Jr. 1976. Visually evoked eye movements in the mouse (Mus musculus). *Vision Res* **16**:1169–1171.

Nahar A, Cho S-H. 2022. Current perspectives in Leber congenital amaurosis type 8 mouse modeling. *Dev Dyn* **251**:1094–1106.
Nikolaou N, Meyer MP. 2015. Lamination speeds the functional development of visual circuits. *Neuron* **88**:999–1013.
Ohama D, Matsuda T, Oinuma I. 2018. Differential regional and subcellular localization patterns of afadin splice variants in the mouse central nervous system. *Brain Res* **1692**:74–86.
Okawa H, Della Santina L, Schwartz GW, Rieke F, Wong ROL. 2014. Interplay of cell-autonomous and nonautonomous mechanisms tailors synaptic connectivity of converging axons in vivo. *Neuron* **82**:125–137.
Pan Y-H, Wu N, Yuan X-B. 2019. Toward a better understanding of neuronal migration deficits in autism spectrum disorders. *Front Cell Dev Biol* **7**:205.
Park C, Falls W, Finger JH, Longo-Guess CM, Ackerman SL. 2002. Deletion in Catna2, encoding alpha N-catenin, causes cerebellar and hippocampal lamination defects and impaired startle modulation. *Nat Genet* **31**:279–284.
Poria D, Dhingra NK. 2015. Spontaneous oscillatory activity in rd1 mouse retina is transferred from ON pathway to OFF pathway via glycinergic synapse. *J Neurophysiol* **113**:420–425.
Puthussery T, Gayet-Primo J, Taylor WR. 2010. Localization of the calcium-binding protein secretagogin in cone bipolar cells of the mammalian retina. *J Comp Neurol* **518**:513–525.
Quiroga RQ, Nadasdy Z, Ben-Shaul Y. 2004. Unsupervised spike detection and sorting with wavelets and superparamagnetic clustering. *Neural Comput* **16**:1661–1687.
Romero DM, Bahi-Buisson N, Francis F. 2018. Genetics and mechanisms leading to human cortical malformations. *Semin Cell Dev Biol* **76**:33–75.
Sakakibara S, Maruo T, Miyata M, Mizutani K, Takai Y. 2018. Requirement of the F-actin-binding activity of l-afadin for enhancing the formation of adherens and tight junctions. *Genes Cells* **23**:185–199.
Sato S, Inoue T, Terada K, Matsuo I, Aizawa S, Tano Y, Fujikado T, Furukawa T. 2007. Dkk3-Cre BAC transgenic mouse line: a tool for highly efficient gene deletion in retinal progenitor cells. *Genesis* **45**:502–507.
Sato T, Fujita N, Yamada A, Ooshio T, Okamoto R, Irie K, Takai Y. 2006. Regulation of the assembly and adhesion activity of E-cadherin by nectin and afadin for the formation of adherens junctions in Madin-Darby canine kidney cells. *J Biol Chem* **281**:5288–5299.
Scalabrino ML, Thapa M, Chew LA, Zhang E, Xu J, Sampath AP, Chen J, Field GD. 2022. Robust cone-mediated signaling persists late into rod photoreceptor degeneration. *Elife* **11**. doi:10.7554/eLife.80271
Schmucker C, Seeliger M, Humphries P, Biel M, Schaeffel F. 2005. Grating acuity at different luminances in wild-type mice and in mice lacking rod or cone function. *Invest Ophthalmol Vis Sci* **46**:398–407.
Sebbagh M, Schwartz MA. 2024. Afadin-nectin forces its way to the front. *J Cell Biol* **223**. doi:10.1083/jcb.202403177
Shen N, Wang B, Soto F, Kerschensteiner D. 2020. Homeostatic plasticity

shapes the retinal response to photoreceptor degeneration. *Curr Biol* **30**:1916-1926.e3.
Shen W, Fruttiger M, Zhu L, Chung SH, Barnett NL, Kirk JK, Lee S, Coorey NJ, Killingsworth M, Sherman LS, Gillies MC. 2012. Conditional Müller cell ablation causes independent neuronal and vascular pathologies in a novel transgenic model. *J Neurosci* **32**:15715–15727.
Solovei I, Kreysing M, Lanctôt C, Kösem S, Peichl L, Cremer T, Guck J, Joffe B. 2009. Nuclear architecture of rod photoreceptor cells adapts to vision in mammalian evolution. *Cell* **137**:356–368.
Stouffer MA, Golden JA, Francis F. 2016. Neuronal migration disorders: Focus on the cytoskeleton and epilepsy. *Neurobiol Dis* **92**:18–45.
Strettoi E, Di Marco B, Orsini N, Napoli D. 2022. Retinal plasticity. *Int J Mol Sci* **23**:1138.
Stuck MW, Conley SM, Naash MI. 2012. Defects in the outer limiting membrane are associated with rosette development in the Nrl-/- retina. *PLoS One* **7**:e32484.
Tachibana K, Nakanishi H, Mandai K, Ozaki K, Ikeda W, Yamamoto Y, Nagafuchi A, Tsukita S, Takai Y. 2000. Two cell adhesion molecules, nectin and cadherin, interact through their cytoplasmic domain-associated proteins. *J Cell Biol* **150**:1161–1176.
Takai Y, Ikeda W, Ogita H, Rikitake Y. 2008a. The immunoglobulin-like cell adhesion molecule nectin and its associated protein afadin. *Annu Rev Cell Dev Biol* **24**:309–342.
Takai Y, Miyoshi J, Ikeda W, Ogita H. 2008b. Nectins and nectin-like molecules: roles in contact inhibition of cell movement and proliferation. *Nat Rev Mol Cell Biol* **9**:603–615.
Takai Y, Nakanishi H. 2003. Nectin and afadin: novel organizers of intercellular junctions. *J Cell Sci* **116**:17–27.
Takeuchi H, Horie S, Moritoh S, Matsushima H, Hori T, Kimori Y, Kitano K, Tsubo Y, Tachibana M, Koike C. 2018. Different activity patterns in retinal ganglion cells of TRPM1 and mGluR6 knockout mice. *Biomed Res Int* **2018**:2963232.
Tanimoto N, Sothilingam V, Kondo M, Biel M, Humphries P, Seeliger MW. 2015. Electroretinographic assessment of rod- and cone-mediated bipolar cell pathways using flicker stimuli in mice. *Sci Rep* **5**:10731.
Thaung C, Arnold K, Jackson IJ, Coffey PJ. 2002. Presence of visual head tracking differentiates normal sighted from retinal degenerate mice. *Neurosci Lett* **325**:21–24.
The electroretinogram: ERG by Ido Perlman. n.d. https://webvision.med.utah.edu/book/electrophysiology/the-electroretinogram-erg/
Ueno A, Omori Y, Sugita Y, Watanabe S, Chaya T, Kozuka T, Kon T, Yoshida S, Matsushita K, Kuwahara R, Kajimura N, Okada Y, Furukawa T. 2018. Lrit1, a retinal transmembrane protein, regulates selective synapse formation in cone photoreceptor cells and visual acuity. *Cell Rep* **22**:3548–3561.
Veeraval L, O'Leary CJ, Cooper HM. 2020. Adherens junctions: Guardians of

cortical development. *Front Cell Dev Biol* **8**:6.
Warwick RA, Riccitelli S, Heukamp AS, Yaakov H, Swain BP, Ankri L, Mayzel J, Gilead N, Parness-Yossifon R, Di Marco S, Rivlin-Etzion M. 2024. Top-down modulation of the retinal code via histaminergic neurons of the hypothalamus. *Sci Adv* **10**:eadk4062.
Wässle H. 2004. Parallel processing in the mammalian retina. *Nat Rev Neurosci* **5**:747–757.
Willbold E, Layer PG. 1998. Müller glia cells and their possible roles during retina differentiation in vivo and in vitro. *Histol Histopathol* **13**:531–552.
Xu H, Enemchukwu N, Zhong X, Zhang O, Fu Y. 2020. Deletion of M-opsin prevents M cone degeneration in a mouse model of Leber congenital amaurosis. *Am J Pathol* **190**:1059–1067.
Yamamoto H, Kon T, Omori Y, Furukawa T. 2020. Functional and evolutionary diversification of Otx2 and Crx in vertebrate retinal photoreceptor and bipolar cell development. *Cell Rep* **30**:658-671.e5.
Yamasaki S, Tu H-Y, Matsuyama T, Horiuchi M, Hashiguchi T, Sho J, Kuwahara A, Kishino A, Kimura T, Takahashi M, Mandai M. 2022. A Genetic modification that reduces ON-bipolar cells in hESC-derived retinas enhances functional integration after transplantation. *iScience* **25**:103657.
Ye M, Huang J, Mou Q, Luo J, Hu Y, Lou X, Yao K, Zhao B, Duan Q, Li X, Zhang H, Zhao Y. 2021. CD82 protects against glaucomatous axonal transport deficits via mTORC1 activation in mice. *Cell Death Dis* **12**:1149.
Zapp SJ, Nitsche S, Gollisch T. 2022. Retinal receptive-field substructure: scaffolding for coding and computation. *Trends Neurosci* **45**:430–445.
Zhadanov AB, Provance DW Jr, Speer CA, Coffin JD, Goss D, Blixt JA, Reichert CM, Mercer JA. 1999. Absence of the tight junctional protein AF-6 disrupts epithelial cell-cell junctions and cell polarity during mouse development. *Curr Biol* **9**:880–888.
Zhang P-M, Wu J-Y, Zhou Y, Liang P-J, Yuan J-Q. 2004. Spike sorting based on automatic template reconstruction with a partial solution to the overlapping problem. *J Neurosci Methods* **135**:55–65.

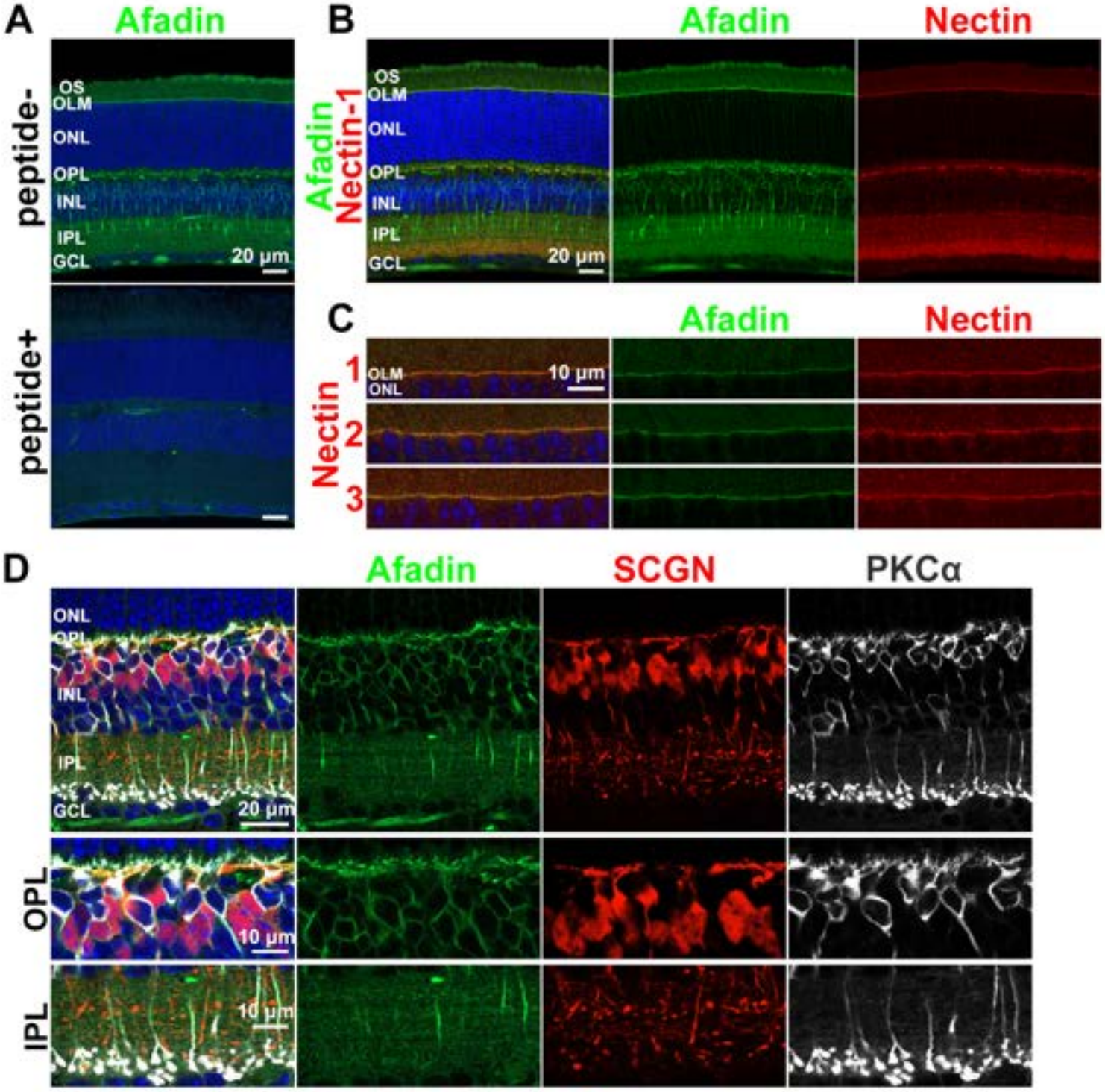
A
Afadin
peptide-
peptide+
OS
OLM
ONL
OPL
INL
IPL
GCL
20 µm
B
Afadin
Nectin
Afadin
Nectin-1
OS
OLM
ONL
OPL
INL
IPL
GCL
20 µm
C
Afadin
Nectin
Nectin
1
2
3
OLM
ONL
10 µm
D
Afadin
SCGN
PKCα
ONL
OPL
INL
IPL
GCL
20 µm
OPL
10 µm
IPL
10 µm

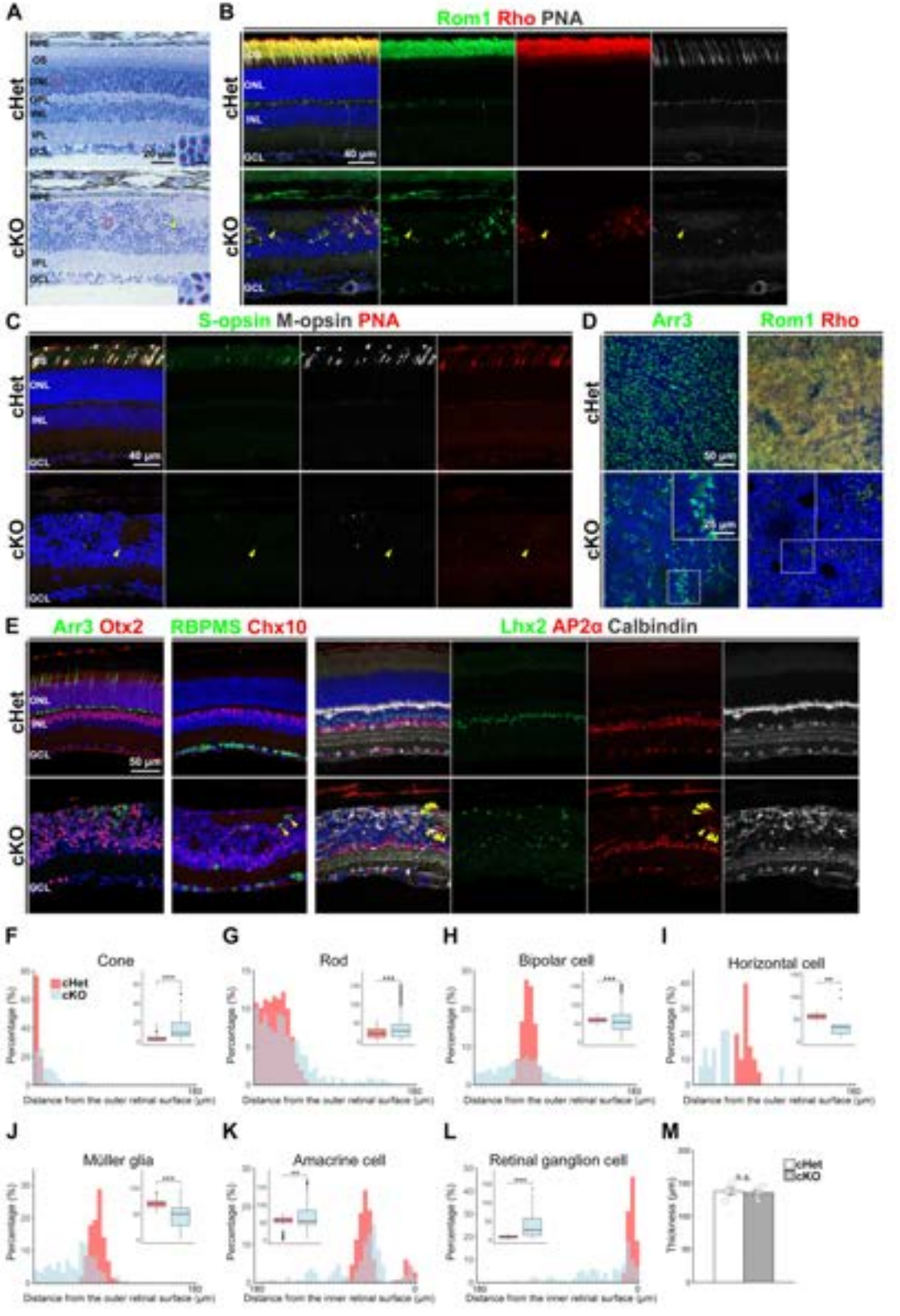
A
cHet
cKO
RPE
OS
ONL
OPL
INL
IPL
GCL
20 μm
B
Rom1 Rho PNA
cHet
cKO
ONL
INL
GCL
40 μm
C
S-opsin M-opsin PNA
cHet
cKO
ONL
INL
GCL
40 μm
D
Arr3
Rom1 Rho
cHet
cKO
50 μm
20 μm
E
Arr3 Otx2
RBPMS Chx10
Lhx2 AP2α Calbindin
cHet
cKO
ONL
INL
GCL
50 μm
F
Cone
cHet
cKO
Percentage (%)
Distance from the outer retinal surface (μm)
G
Rod
Percentage (%)
Distance from the outer retinal surface (μm)
H
Bipolar cell
Percentage (%)
Distance from the outer retinal surface (μm)
I
Horizontal cell
Percentage (%)
Distance from the outer retinal surface (μm)
J
Müller glia
Percentage (%)
Distance from the outer retinal surface (μm)
K
Amacrine cell
Percentage (%)
Distance from the inner retinal surface (μm)
L
Retinal ganglion cell
Percentage (%)
Distance from the inner retinal surface (μm)
M
cHet
cKO
Thickness (μm)
n.s.

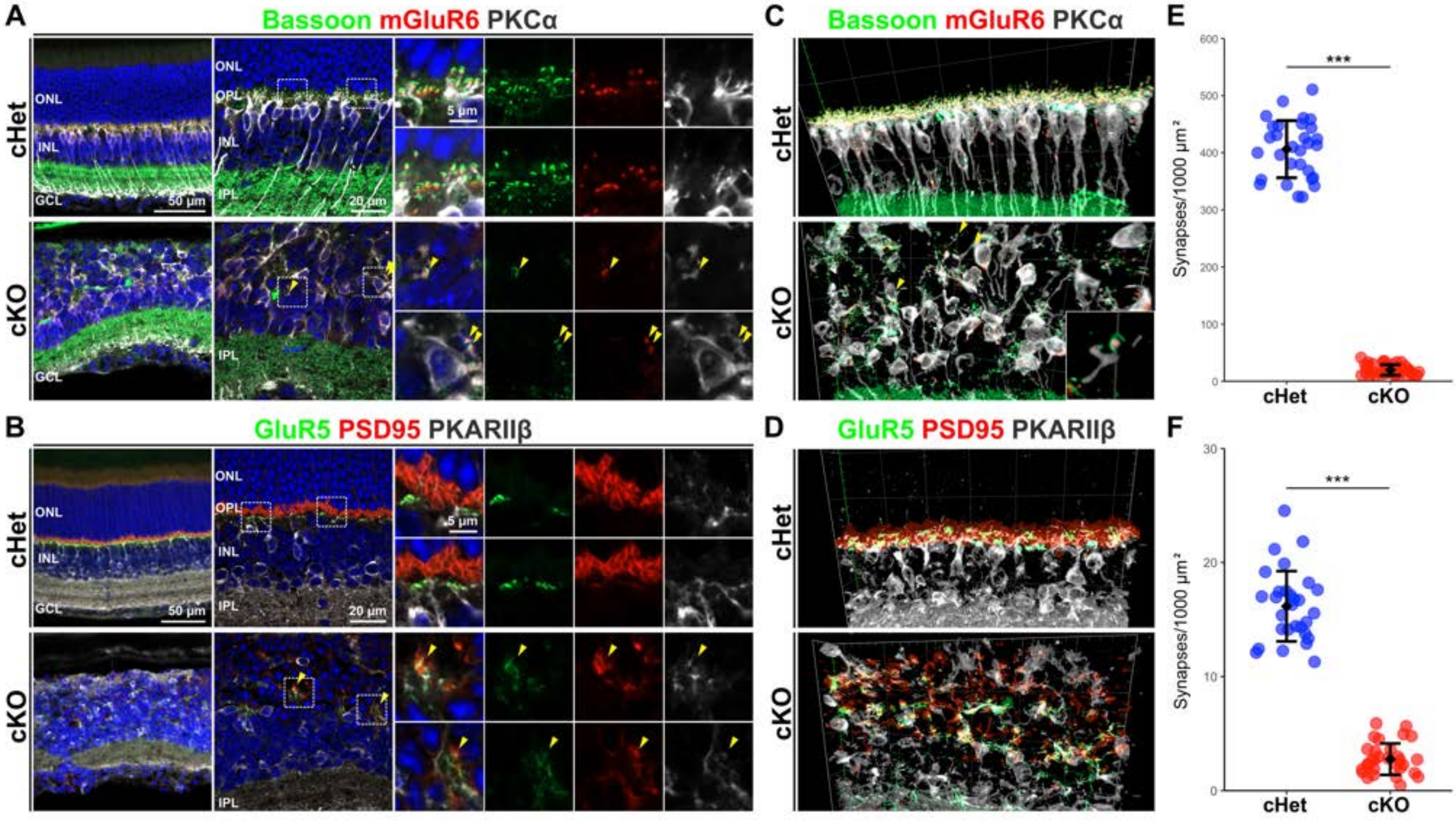
A
Bassoon mGluR6 PKCα
cHet
cKO
ONL
INL
GCL
OPL
IPL
50 µm
20 µm
5 µm
B
GluR5 PSD95 PKARIIβ
C
D
E
F
Synapses/1000 µm²
***
cHet
cKO

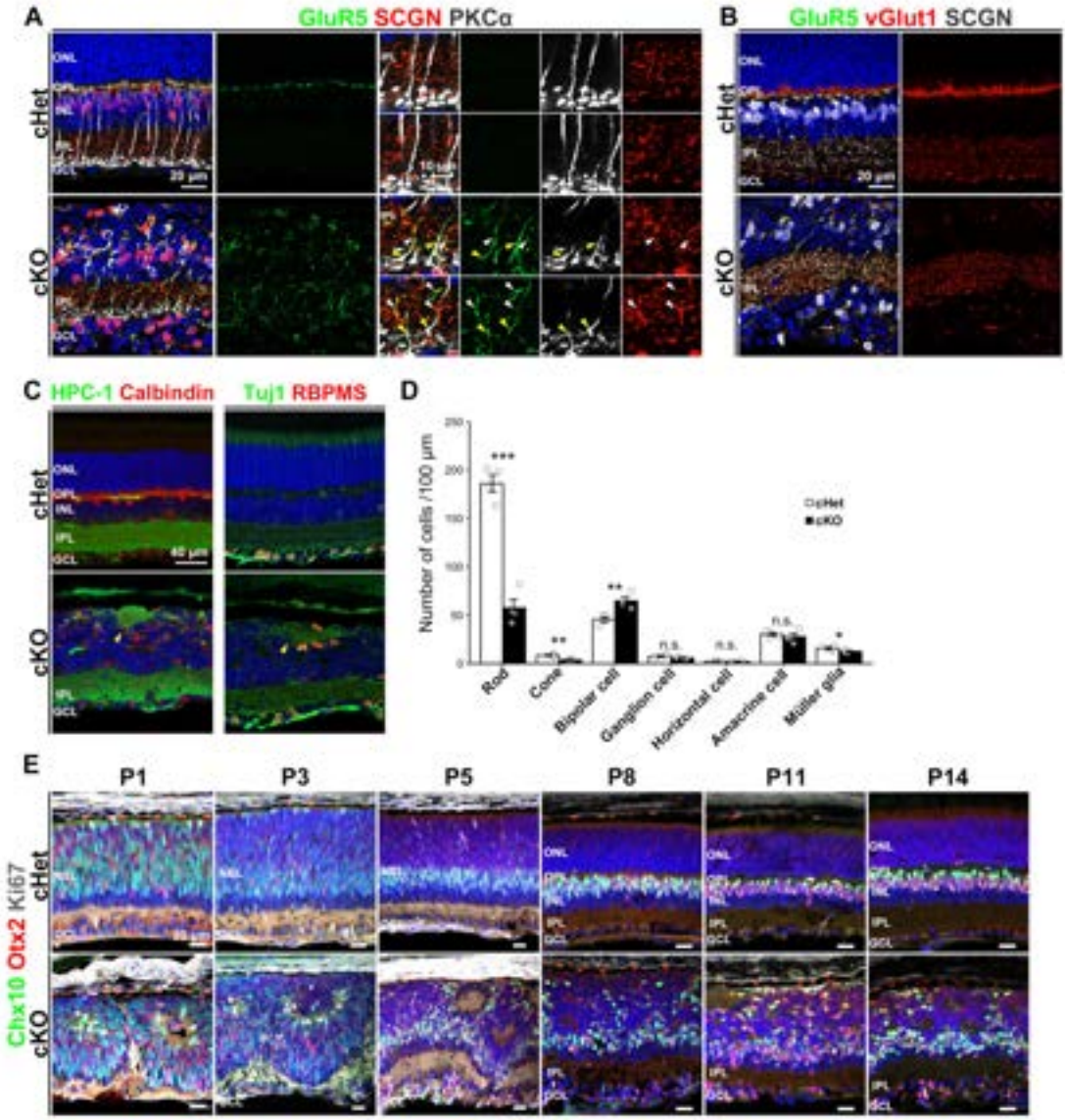
A
GluR5 SCGN PKCα
cHet
cKO
ONL
OPL
INL
IPL
GCL
20 μm
10 μm
B
GluR5 vGlut1 SCGN
C
HPC-1 Calbindin
Tuj1 RBPMS
40 μm
D
Number of cells /100 μm
cHet
cKO
***
**
n.s.
*
Rod
Cone
Bipolar cell
Ganglion cell
Horizontal cell
Amacrine cell
Müller glia
E
P1
P3
P5
P8
P11
P14
Chx10 Otx2 Ki67

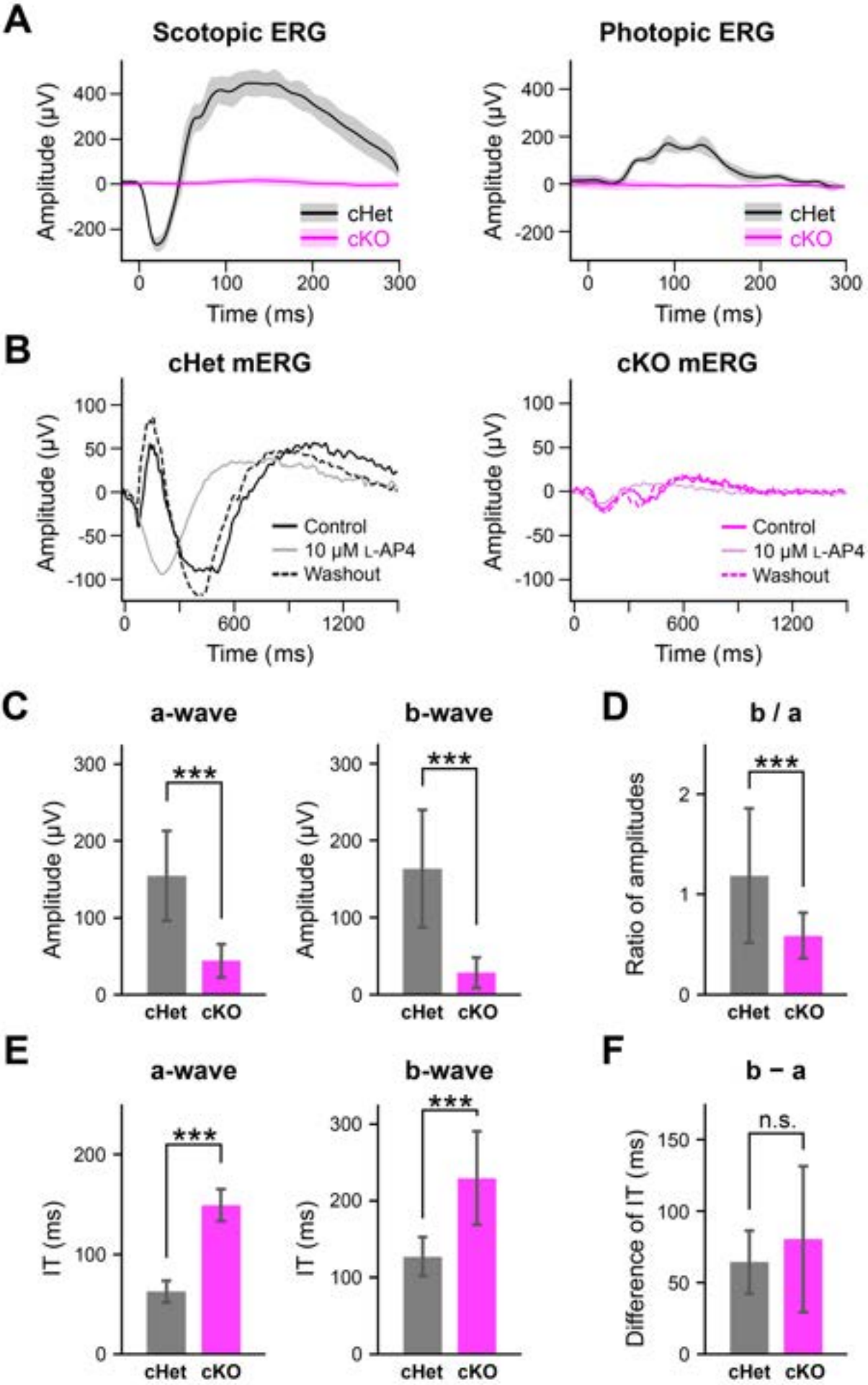
A
Scotopic ERG
Photopic ERG
Amplitude (μV)
Time (ms)
cHet
cKO
B
cHet mERG
cKO mERG
Control
10 μM L-AP4
Washout
C
a-wave
b-wave
D
b / a
Ratio of amplitudes
E
IT (ms)
F
b − a
Difference of IT (ms)
n.s.
***

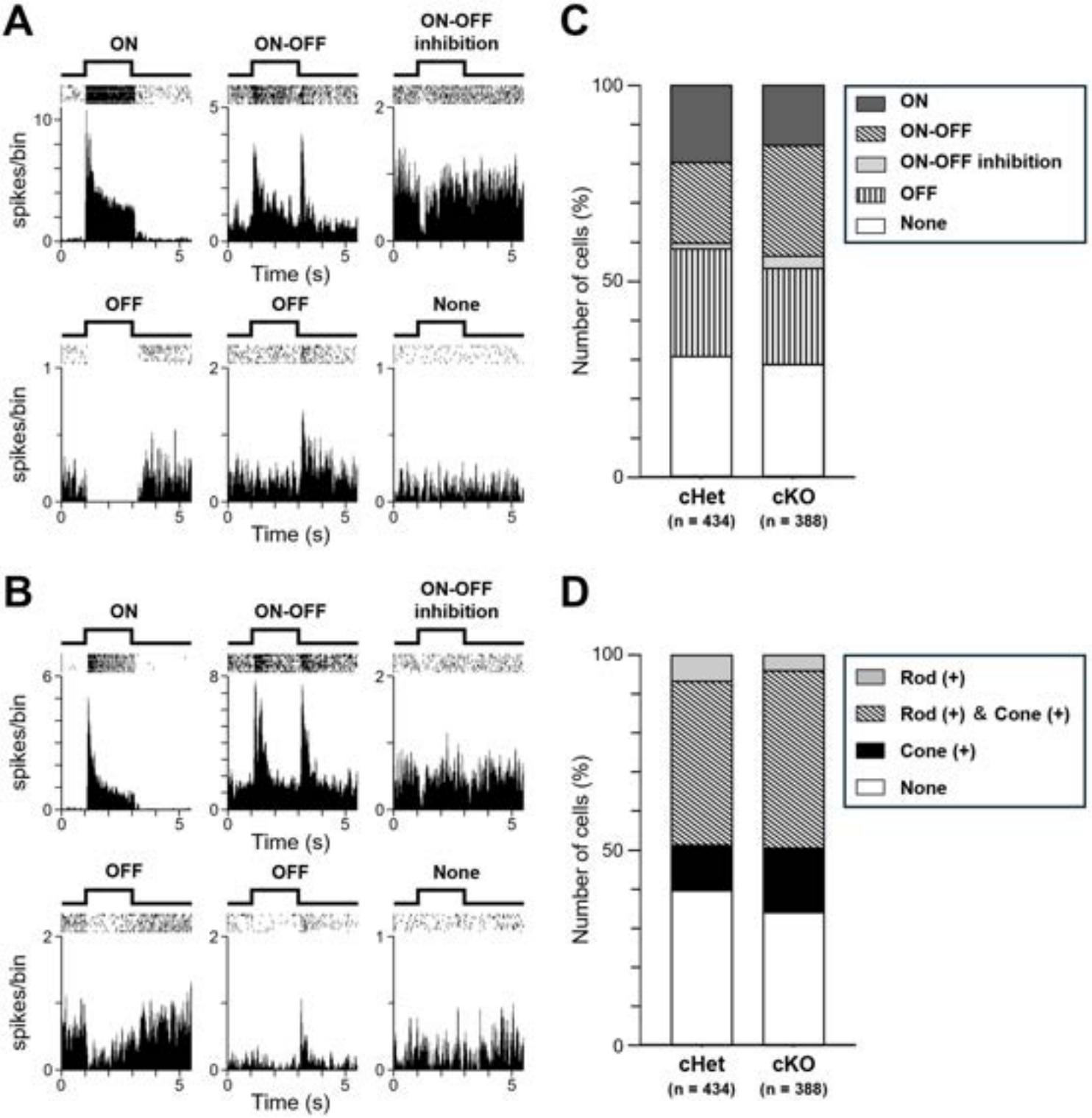
A
ON
ON-OFF
ON-OFF inhibition
OFF
OFF
None
spikes/bin
Time (s)
B
ON
ON-OFF
ON-OFF inhibition
OFF
OFF
None
spikes/bin
Time (s)
C
Number of cells (%)
ON
ON-OFF
ON-OFF inhibition
OFF
None
cHet
(n = 434)
cKO
(n = 388)
D
Number of cells (%)
Rod (+)
Rod (+) & Cone (+)
Cone (+)
None
cHet
(n = 434)
cKO
(n = 388)

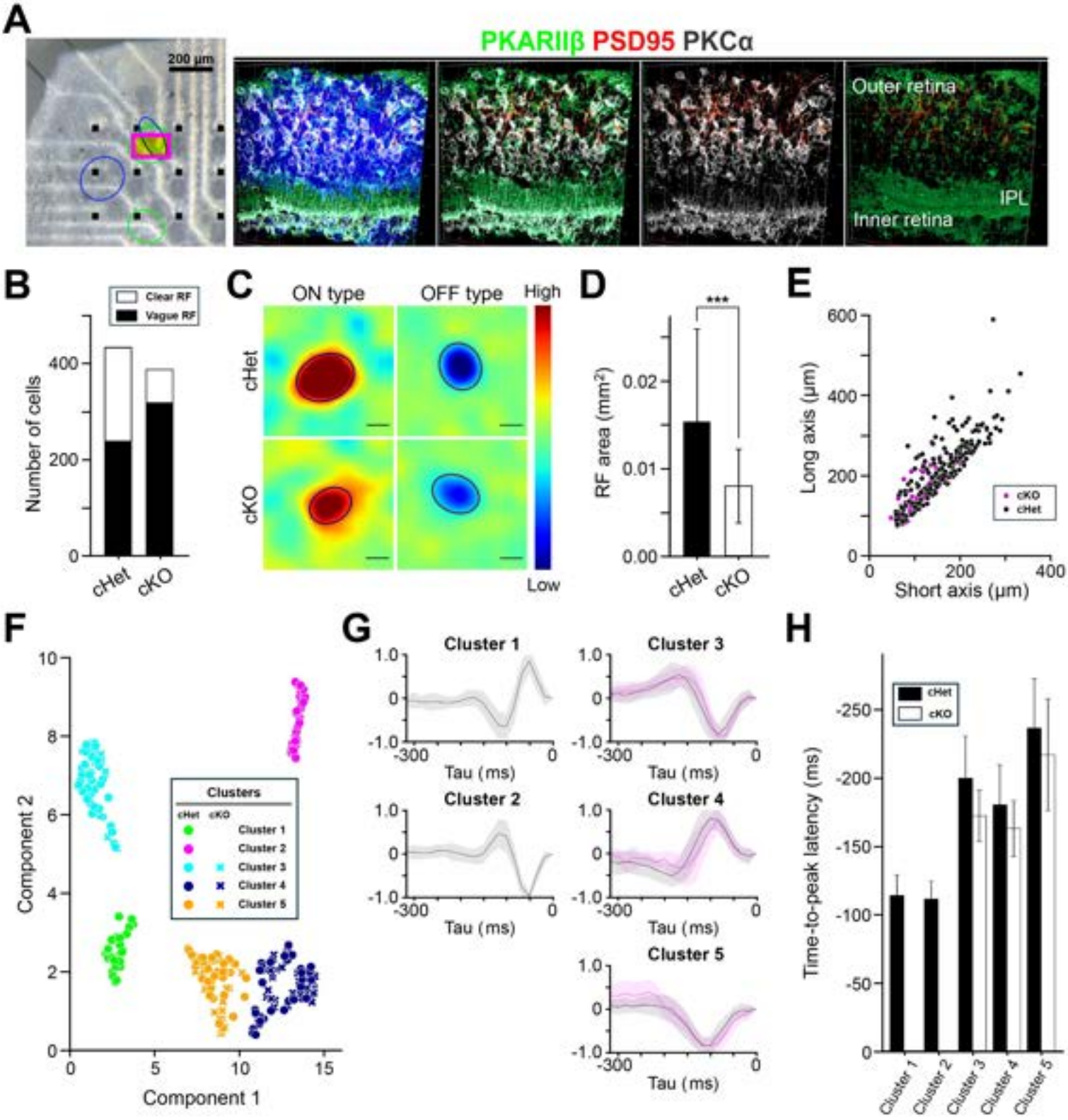
A
200 µm
PKARIIβ PSD95 PKCα
Outer retina
IPL
Inner retina
B
Clear RF
Vague RF
Number of cells
cHet
cKO
C
ON type
OFF type
High
Low
cHet
cKO
D
***
RF area (mm²)
cHet
cKO
E
Long axis (µm)
Short axis (µm)
cKO
cHet
F
Component 2
Component 1
Clusters
cHet cKO
Cluster 1
Cluster 2
Cluster 3
Cluster 4
Cluster 5
G
Cluster 1
Cluster 2
Cluster 3
Cluster 4
Cluster 5
Tau (ms)
H
cHet
cKO
Time-to-peak latency (ms)
Cluster 1
Cluster 2
Cluster 3
Cluster 4
Cluster 5

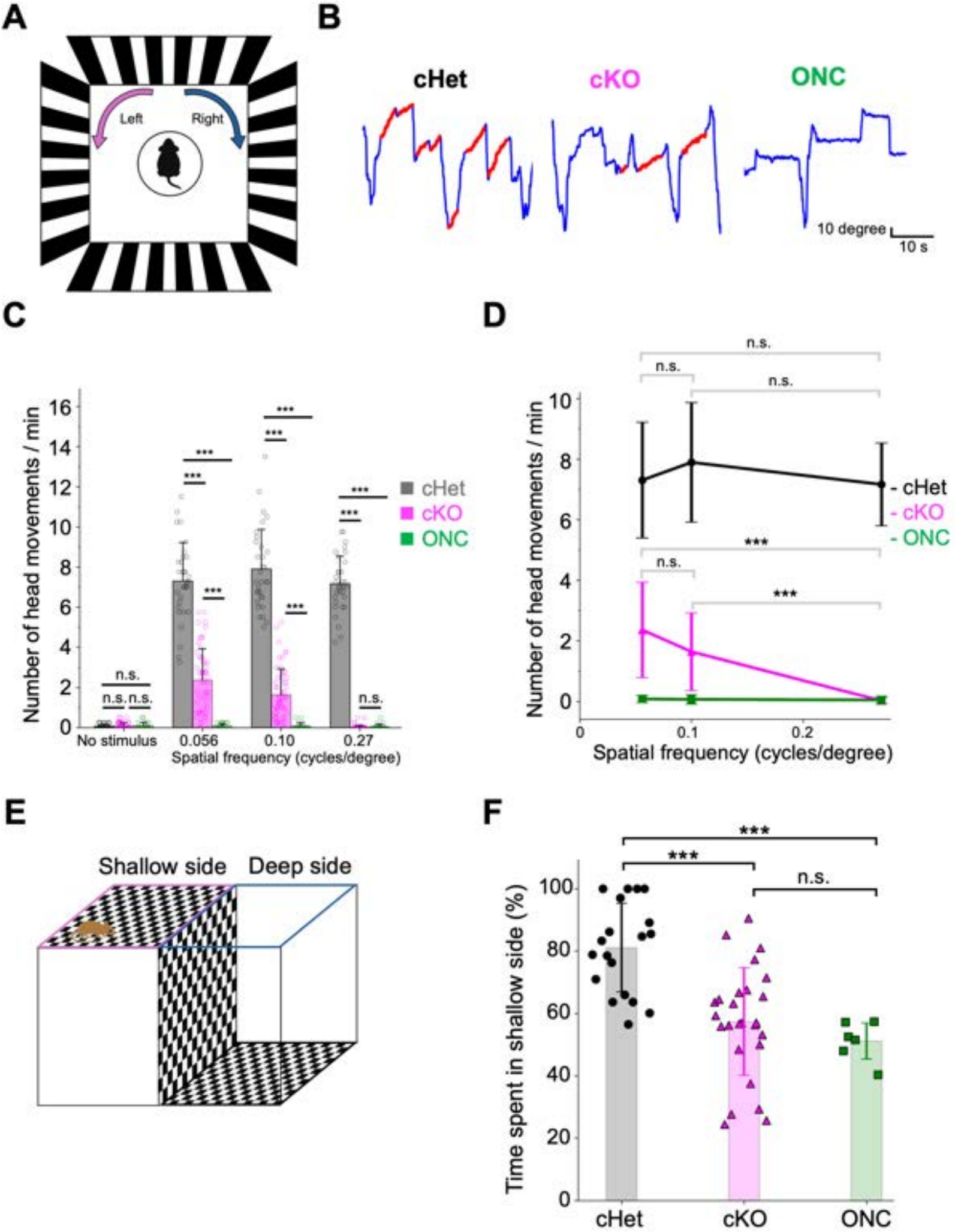
A
Left
Right
B
cHet
cKO
ONC
10 degree
10 s
C
Number of head movements / min
cHet
cKO
ONC
n.s.
***
No stimulus
0.056
0.10
0.27
Spatial frequency (cycles/degree)
D
Number of head movements / min
- cHet
- cKO
- ONC
Spatial frequency (cycles/degree)
E
Shallow side
Deep side
F
Time spent in shallow side (%)
cHet
cKO
ONC

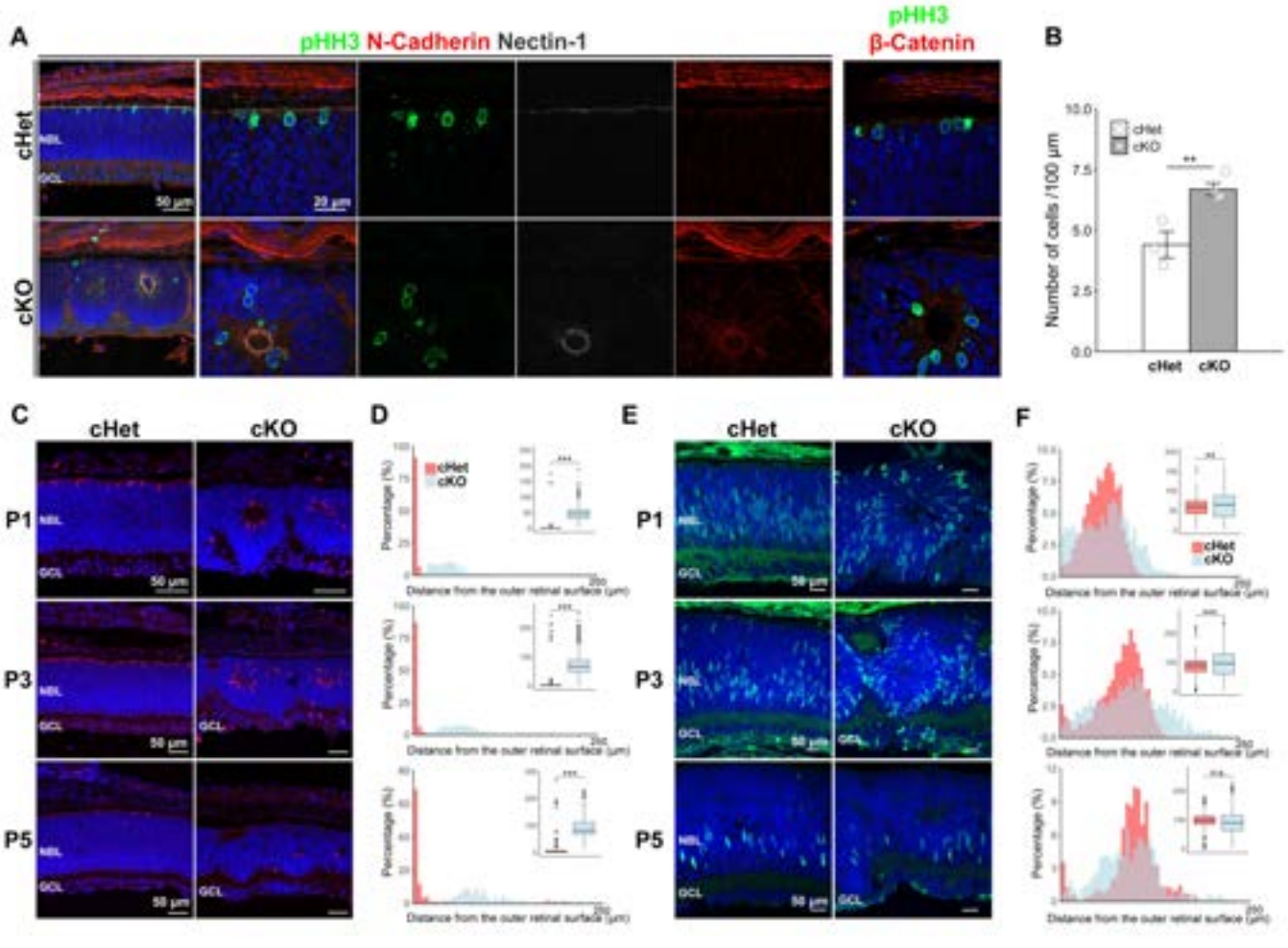
A
pHH3 N-Cadherin Nectin-1
pHH3
β-Catenin
cHet
cKO
NBL
GCL
50 µm
20 µm
B
Number of cells /100 µm
cHet
cKO
C
cHet
cKO
P1
P3
P5
D
Percentage (%)
Distance from the outer retinal surface (µm)
E
F